AIAA SciTech Forum
January 3-7, 2022, San Diego, CA & Virtual
AIAA SCITECH 2022 Forum

10.2514/6.2022-0686

Development of a Multi-fidelity Design, Analysis, and Optimization Environment for Future Transport Aircraft *

S. Karpuk†, V. Mosca‡, C. Liu§ and A. Elham¶
Technische Universitat Braunschweig, Braunschweig, Germany, 38108

Present work describes the development of a multi-fidelity aircraft design, analysis, and optimization environment for future airplanes being developed under the Cluster of Excellence SE^{2}A (Sustainable and Energy-Efficient Aviation). The framework, named ADEMAO (Aircraft Design Engine based on Multidisciplinary Analysis and Optimization), is a multi-layer design environment that can support the aircraft design from clean sheet sizing to high-fidelity multi-disciplinary design optimization. ADEMAO is specially developed to support the integration of novel airframe and energy network technologies for the design of low (zero) emission aircraft. Especial attention is paid to the design and optimization of electric/hybrid-electric aircraft. In this paper, different layers of ADEMAO and the connection among them, as well as the methods and tools available for each design block, are described. Capabilities of the software are thoroughly described and supported with example design cases of three reference aircraft considered under the research cluster.

I. Nomenclature

α	=	angle-of-attack (AoA)
γ	=	leading edge sweep angle
ϵ	=	twist angle
η_{total}	=	total efficiency
λ	=	taper ratio
$\Lambda_{C/4}$	=	quarter-chord sweep
AR	=	aspect ratio
BLS	=	boundary layer suction
b	=	wing span
C_D	=	drag coefficient
C_L	=	lift coefficient
C_r	=	root chord
C_t	=	tip chord
D_{rest}	=	rest drag
DOC	=	direct operating costs
E^*	=	energy density
g	=	gravitational acceleration
H	=	altitude
$HLFC$	=	hybrid laminar flow control
K	=	drag penalty coefficient
L_δ	=	roll moment due to aileron deflection
L/D	=	lift-to-drag ratio

*This submission is intended for the special session SE^{2}A – Sustainable and Energy Efficient Aviation.

†PhD candidate, Institute of Aircraft Design and Lightweight Structures, Cluster of Excellence SE^{2}A – Sustainable and Energy-Efficient Aviation, s.karpuk@tu-braunschweig.de.

‡PhD candidate, Institute of Aircraft Design and Lightweight Structures, Cluster of Excellence SE^{2}A – Sustainable and Energy-Efficient Aviation, v.mosca@tu-braunschweig.de.

§Postdoc Researcher, Institute of Aircraft Design and Lightweight Structures, chuanzhen.liu@tu-braunschweig.de

¶Professor, Institute of Aircraft Design and Lightweight Structures, Cluster of Excellence SE^{2}A – Sustainable and Energy-Efficient Aviation, a.elham@tu-braunschweig.de.

$m_{battery}$	=	battery mass
m_{CO_2}	=	equivalent CO_2 emission mass
n	=	load factor
P/W	=	power-to-weight ratio
R	=	range
R_{LE}	=	leading edge radius
S_{wing}	=	wing area
t	=	panel thickness
t/c	=	airfoil thickness
W_0	=	maximum take-off weight (MTOW)
W_e	=	operating empty weight (OEW)
W_{des}	=	design weight
W_b	=	battery weight
W_f	=	fuel weight
W_w	=	wing weight
ZFW	=	zero fuel weight
z	=	Z-coordinate

II. Introduction

Significant climate changes and potential environmental impact due to increased transportation in the near future have motivated many industries to reduce CO_2 and NO_x emissions. As a major transportation method, the aviation industry also follows the trend to reduce the emission of new generations of aircraft. Improvements in airframe and engine technologies increase aircraft efficiency and reduce their emission. However, a potential increase in air transportation may still lead to an increase in overall CO_2 and NO_x emission. Based on the Flightpath 2050 [1], challenging recommendations to reduce aircraft's total emission was proposed. However, satisfying given goals does not seem to be possible using conventional airframes and propulsion systems, so alternative environmentally-friendly energy sources and novel aircraft concepts must be considered and investigated to understand how potential next-generation aircraft may look like.

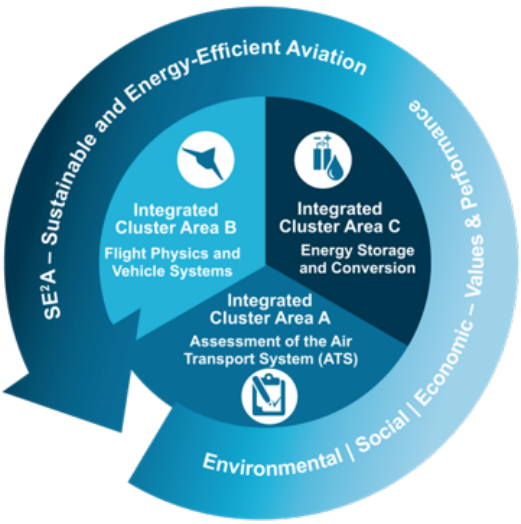

Fig. 1 SE²A cluster structure.

The Cluster of Excellence SE²A (Sustainable and Energy-Efficient Aviation) is focused on the development of next-generation airframe and propulsion technologies, as well as assessment of important operational issues, such as air traffic, noise emission, etc. The cluster is divided into three major branches as shown in Fig. 1. The first branch (ICA A) focuses on the assessment of air transportation systems, their economic and operational future, and their impact on society. The second branch (ICA B) specializes in the development of new airframe technologies and aircraft designs featuring these technologies. Finally, the third group (ICA C) is researching new sustainable and energy-efficient energy sources, conversion, and storage systems.

The ICA B group is divided into four major branches, where the ICA B1 is researching new aerodynamic solutions for next-generation airplanes, such as hybrid laminar flow control (HLFC) and airframe-propulsion interaction such as propeller-wing interaction and boundary layers ingestion (BLI). The ICA B2 is investigating a new solution for passive or active load alleviation using various techniques. ICA B3 is investigating new materials and structure concepts that will enable the integration of new aerodynamic solutions into the airframe and also reduce its weight. Finally, ICA B5 is investigating new aircraft configurations that may maximize the benefits of all technologies considered within the cluster, so the largest benefit from each technology can be achieved.

To analyze aircraft with various technologies and propose configurations that may significantly deviate from conventional airplanes, a multi-fidelity software that can assess various design problems must be developed so that

various non-intuitive design outcomes can be obtained and analyzed during the design process as early as possible. The present research focuses on the development of a multi-layer aircraft design environment that can assess various design problems at different fidelity levels.

Present work is divided into multiple sections. Section 3 describes the general arrangement of the design environment, specific details related to its components, and tools used for each design block. Section 4 presents selected design examples obtained using the design framework to demonstrate the current capabilities of the design environment.

III. The aircraft design and analysis environment structure

A Multi-layer Aircraft Design Framework ADEMAO consists of four blocks that are connected to each other. Each block is responsible for a particular design goal and has a particular fidelity level. The data transition is performed via the Common Parametric Aircraft Configuration Schema (CPACS) [2] for major aircraft features such as geometry, weights, and inertia properties, while separate scripts are used for other more specific components. Such infrastructure enables robust transition between different fidelity analyses and helps gain as much information about the aircraft as possible.

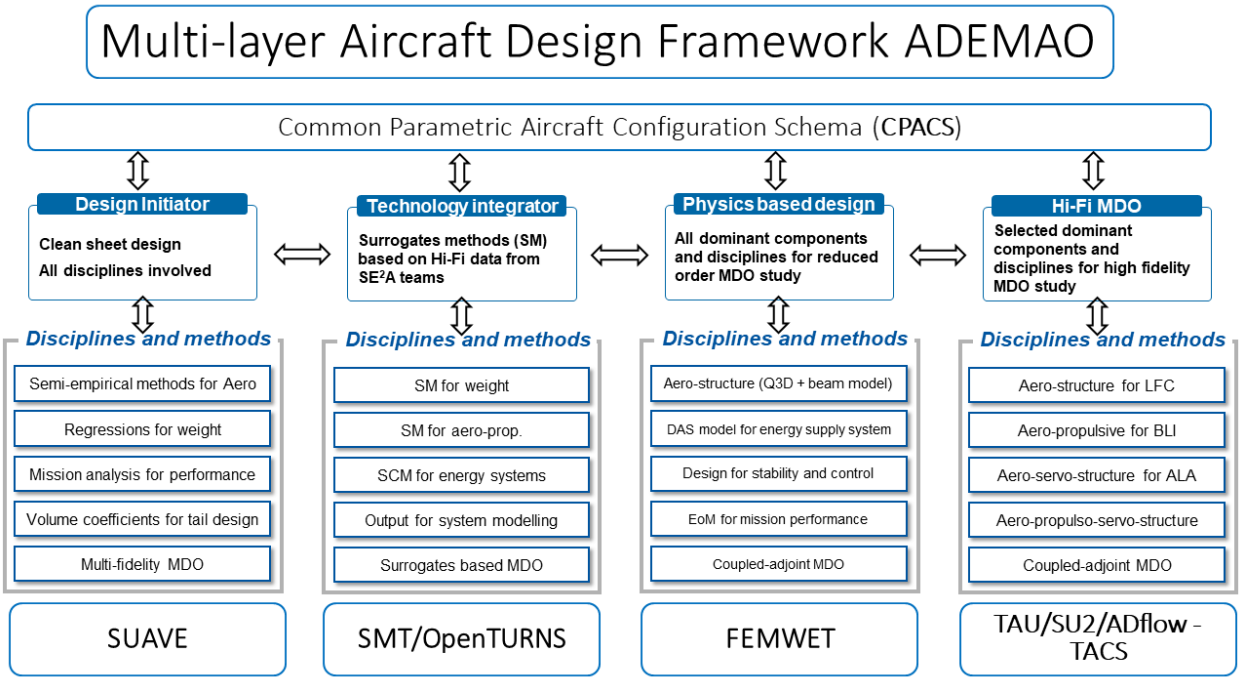

Fig. 2 Structure of the ADEMAO.

A. Block 1: Design initiator

The first block is called the Design Initiator. This block helps initialize an aircraft using available Top-level Requirements and user-defined specifications such as the type of the propulsion system, configuration, and specific technological or airframe features. Stanford University aircraft design environment SUAVE [3] is used as a basis of the design initiator. The default SUAVE features various analysis tools that help estimate aircraft aerodynamics, stability and control characteristics, weights, and mission performance. The multi-fidelity approach is also used in SUAVE, so low-fidelity (fidelity zero) and medium-fidelity (fidelity one) options are available for components such as aerodynamic analysis, aircraft stability analysis, noise analysis, and weights estimation. SUAVE is capable of working with conventional (E)VTOL and high-speed aircraft. Finally, SUAVE can be coupled with multiple optimization algorithms to perform Multi-disciplinary Design Optimization (MDO) analyses. MATLAB/Simulink is used for additional features to support SUAVE during the design process. The design initiator is divided into three major sub-blocks as shown in Fig. 3.

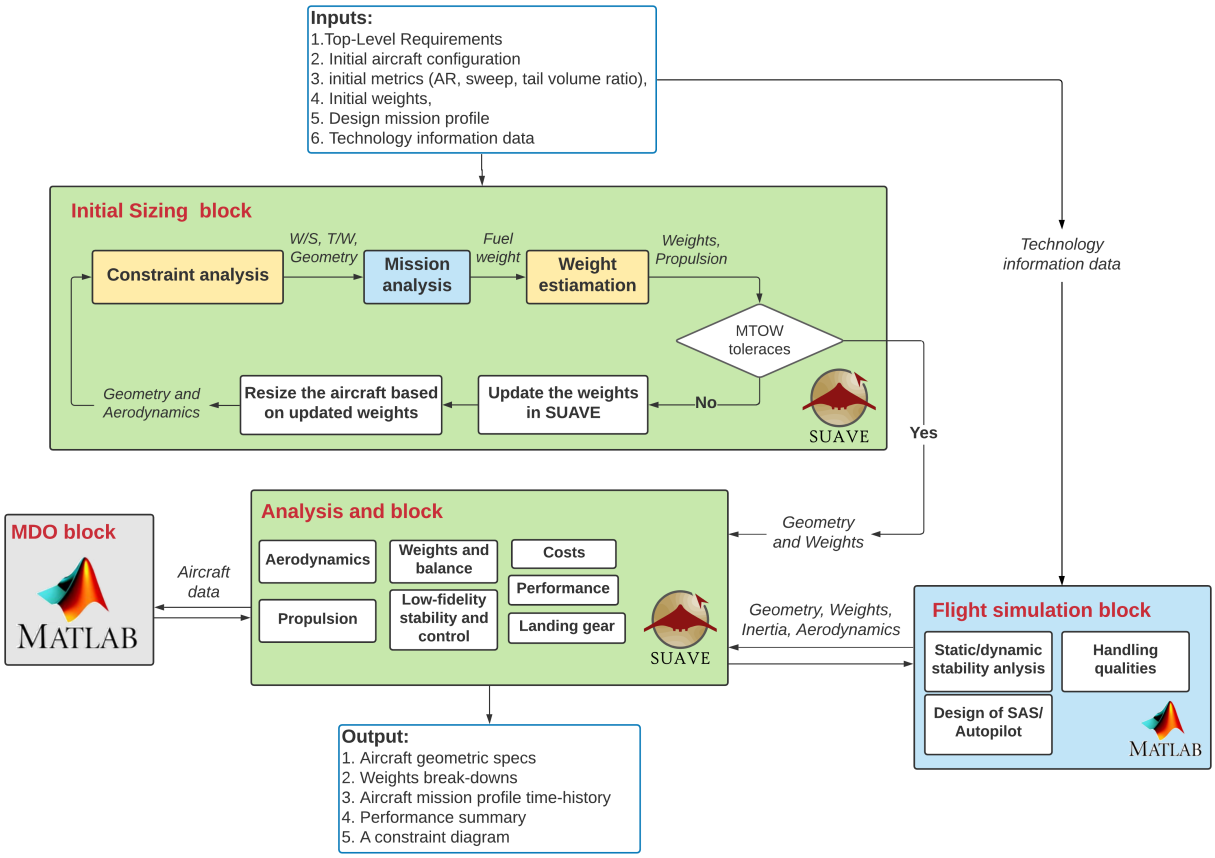

Fig. 3 Initial sizing framework using SUAVE.

The first sub-block is the initial sizing block where the constraint analysis implemented in SUAVE is coupled with the SUAVE mission analysis to have an iterative algorithm to size the aircraft. Sizing iterations are performed based on design thrust-to-weight ratio and the wing loading, which sizes the wing planform and updates aerodynamics and weights of the aircraft. Obtained aerodynamics is fed back to the constraint analysis section to update the design point. The solution converges when the maximum take-off weight reaches the tolerance.

When the aircraft is initially sized, the analysis and refinement sub-block is used for additional aircraft improvements. Various default and extended methods are used to refine the aircraft and perform necessary analysis, which is impossible to do during the initial sizing phase. This sub-block can also export and accept information used in the external MATLAB MDO block, so the refinement process is strengthened with optimization algorithms.

The design initiator features an in-house developed flight simulator using MATLAB/Simulink. The simulator is capable of simulating both jet and propeller-driven aircraft, although the engine modeling fidelity is currently low, although multiple low-fidelity models are included in the simulator. The aerodynamic analysis is based on semi-empirical formulations of the vortex-lattice method using AVL [4]. Various high-lift devices options are added to the simulator to extend the simulation capabilities of AVL.

Finally, after the initial design is completed, all information is post-processed in terms of data files and the CPACS model, which is used for other design blocks and by other cluster groups.

To enable a more universal application of the framework for unconventional aircraft, several existing SUAVE methods were extended, and additional modules were developed.

1. Constraint analysis

A constraint analysis block was implemented to perform initial aircraft sizing and couple both the constraint diagram and the mission analysis to obtain a robust design initiator. The diagram is available for conventional, hybrid-electric,

and hydrogen aircraft. Constraints equations are based on derivations provided by Gudmundsson [5]. Formulations of the propulsion system thrust or power lapse include various methods for more design flexibility and investigation of design sensitivities to applied methods. Methods of Howe [6], Mattingly [7], Scholz [8], and Bartel [9] were implemented as available options. The Oswald efficiency model of Scholz [10] was implemented to have a dependence of the wing taper and aspect ratios. Aerodynamic coefficients required for the constraint analysis can be either prescribed by the user or extracted from the SUAVE mission analysis to couple both analyses into one process. Details about the constraint and mission analyses coupling are described in the following section.

2. Aerodynamics

The default SUAVE features numerous methods for aerodynamic analysis to achieve a multi-fidelity analysis approach. An additional medium-fidelity Quasi-3D [11] method was introduced as an extension of existing SUAVE methods. The method combines three-dimensional analysis of AVL and airfoil analysis using Xfoil [12] or MSES [13] to determine the wing lift and drag which has higher accuracy than semi-empirical formulations but does not require significant computational power as high-fidelity CFD methods.

In addition, additional aerodynamic formulations of high-lift devices using methods of Torenbeek [14] and Roskam [15] were introduced into SUAVE to have more flexibility in terms of high-lift devices selection and analysis. All required charts were digitized to obtain surrogate models that can be rapidly used during the aircraft sizing and refinement.

3. Propulsion

Two additional energy networks were implemented within SUAVE. A parallel hybrid-electric energy network was implemented using methods described by Holezen [16], where the energy network depends on the degree of hybridization for power and the operational control parameter which determines the battery utilization strategy. The method was tested on the Se2A medium-range aircraft option with a hybrid-electric propulsion system to investigate the influence of advanced airframe technologies on the applicability of such aircraft.

The second energy network implemented in SUAVE is the hydrogen fuel-cell model using the method of [17, 18]. The method was implemented during the conceptual design of a general-aviation hydrogen fuel cell aircraft with distributed propulsion capabilities to assess potential airframe-propulsion interaction benefits of two technologies [19].

4. Weights

The FLOPS [20] weight estimation method was implemented in SUAVE as the method which is capable of working with both conventional and unconventional configurations. Moreover, the method was extended to estimate the weights of various energy networks. Methods for the hydrogen fuel tank weight estimation from Verstraete [21] and Brewer [22] were integrated into FLOPS for hydrogen combustion and hydrogen fuel-cell networks. For hybrid-electric aircraft, weight estimations for high-power superconducting electric motors and gearboxes of various technological advancements were implemented for hybrid-electric energy networks.

Moreover, a medium-fidelity wing weight estimation EMWET [23] was implemented in SUAVE. The method analyzes critical wing load cases using AVL and models a simplified wingbox which is sized according to given limit load requirements. The method was validated for several existing metallic aircraft and showed good agreement with actual results.

Finally, the weight estimation correction for folding wings using the method of Yarigina [24] was introduced in SUAVE as a polynomial fit. The weight penalty is a function of the folding mechanism, the wing insert, and the joint and depends on the spanwise location of the folding mechanism [25].

5. Costs

The costs model described by Hoelzen [16] was implemented in SUAVE since it features both conventional gas-turbine engine cost estimation formulations and includes costs for hybrid-electric energy networks. Additional options to add technology gains based on cluster outcomes were implemented to perform sensitivity studies of costs with respect to technical complexities.

6. Emission

Simplified emission analyses for conventional, hydrogen and electric aircraft were included in SUAVE to investigate the influence of designed aircraft on the emission level. Methods described by Dallara [26] were used to estimate emission of gas turbines powered by kerosene-based or hydrogen fuels, and the method described by Scholz [27] was implemented for electric energy network emission level estimation.

B. Block 2: Surrogate model generator

The second block is related to the generation of surrogate models that help integrate various technologies assessed within the cluster, integrate available data structures (for example, engine maps), or utilize information obtained using high-fidelity tools. Surrogate models of a given data set are generated using the SMT-toolbox [28]. The SMT toolbox features various surrogate modeling methods to create models that can be exported to other framework blocks for more sophisticated design, analysis, and optimization. In addition, the SMT-toolbox is attached to MATLAB to perform internal optimization within the surrogate model data. Finally, for the design initiation block, scripts related to the SMT-toolbox data interpretation and integration were generated, to the surrogate data can be used for the mission analysis and aircraft sizing.

C. Block 3: Physics-based design environment

The third block consists of using physics-based methods as an intermediate level between high and low fidelity. This layer improves the design provided by the first two and generates more detailed information. The framework intends to obtain accurate results keeping low the computational power, integrating different disciplines. The toolbox is used for more detailed optimizations, including boundary layer suction, load alleviation, and aerostructural analysis. For this purpose, the SE^2A full-electric short-range aircraft is optimized considering novel technologies, in particular, Boundary-Layer Suction (BLS) through the use of XFOILSUC [29–31]. A medium-fidelity analysis is also applied to the mid-range aircraft, for this purpose, the coupled-adjoint aerostructural analysis and optimization tool FEMWET [32] is used. FEMWET consists of a quasi-three-dimensional aerodynamic analysis and a finite beam element structural solver coupled together using the Newton method. The aerodynamics module presents a Vortex Lattice Method (VLM) to compute aerodynamic loads and the induced drag, while viscous and wave drag evaluation is performed by a viscous 2D airfoil analysis.

D. Block 4: High-fidelity analysis and optimization

The last layer presents a high-fidelity MDO. In particular, high fidelity analysis is applied when the main configuration parameters are known, and the effect of advanced technologies on selected dominant aircraft components is the subject of the investigation with a high level of accuracy. High fidelity analysis can be applied for aircraft lifting surfaces and structure design through the use of Computational Fluid Dynamics (CFD) and Finite Element Analysis (FEA) products. An example of high fidelity optimization for aerodynamic analysis involves the use of software such as the open-source CFD code ADflow or SU2 tool in order to update the mission analysis implemented in the first layers by the use of surrogate models.

IV. Example cases using the environment

The present section describes multiple design examples generated using the ADEMAO framework within the SE^2A cluster. Four cases are presented: initial sizing and MDO of a short- and mid-range aircraft, Physics-based optimization of the short and mid-range aircraft, high-fidelity aerodynamic optimization of the mid-range aircraft wing for two configurations, and high-fidelity aerodynamic optimization of the long-range blended wing body whose results were used to increase the analysis fidelity of SUAVE. All presented aircraft feature future airframe and propulsion technologies to improve their sustainability. For each configuration, Table 1 describes technological improvements assumptions either obtained from existing references or prescribed by the cluster as the development goal. At early design stages, given assumptions were considered as multiplication factors that are introduced into particular analysis components.

Table 1 Technologies used under the SE^{2}A SR cluster and their corresponding assumptions.

	Aircraft type		
Technology	**Short-range**	**Mid-range**	**Long-range**
Laminar flow control	70% laminar flow on the wing or until the shock fuselage is laminar until the wing-body fairing		
Load alleviation	Limit load factor of 2.0		
Advanced materials and structure concepts	Structural weight is reduced by 20%		
Boundary layer ingestion	-	Reduction in SFC by 5%	
Ultra-high bypass ratio turbofan engines	-	Reduction in SFC by 25%	
Superconducting electric motors	High-temperature Superconducting motors		-
High-energy-density batteries	Assumptions are based on research		-

A. Short-range and mid-range aircraft conceptual designs

First examples include the initialization process of short- and mid-range aircraft considered for the Excellence cluster. Initial sizing, initial trade studies, and a series of low-fidelity MDO were performed for both airplanes. The section describes preliminary design results and findings related to each configuration.

1. Initial sizing of the SE^{2}A Short-range aircraft

The goal of the short-range aircraft design was to investigate the capabilities of advanced technologies to introduce an all-electric aircraft with TLRs similar to ATR-72 [33] by 2050. A set of top-level requirements is shown in Table 2.

Table 2 SE^{2}A SR Top-level requirements.

Requirement	**Value**	**Units**
Design range for maximum payload	926	km
Maximum payload	7500	kg
Cruise Mach number	0.42	
Service ceiling	7620	m
Take-off field length	1400	m
Landing distance	1100	m
Certification	CS-25 [34]	

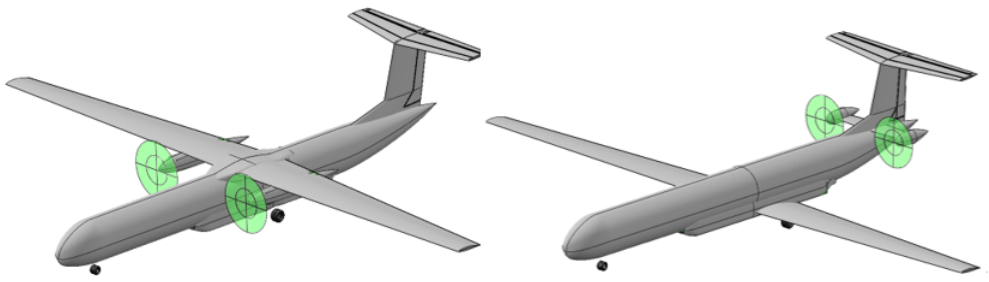

Fig. 4 Configuration of the SE^{2}A SR aircraft.

The initial sizing process was performed using the constraint analysis and the SUAVE mission analysis. Two aircraft configurations were considered for the concept selection: a conventional configuration with a top-wing and

wing-mounted engines and a low-wing with aft-fuselage mounted engines. Fig. 4 shows the configurations generated in OpenVSP [35]. For each configuration, initial parametric sensitivities to the wing aspect ratio and wing loading were performed to investigate general trends of the aircraft and select the configuration with the best-desired characteristics. Fig. 5 shows a sample aircraft trade study with respect to the aircraft wing loading and aspect ratio for the configuration with aft-mounted engines. The main selection criterion was the aircraft DOC. Based on the initial sizing and sensitivity, the aircraft corresponding to minimum DOC was selected, and finally, two airplanes with the best values of DOC were compared to select the configuration which offered the smallest costs. It was important to notice the effect of wing folding on aircraft weights and operating costs. When the folding penalty is introduced, a significant increase in weights and operating costs are present. Consequently, folding needs to be considered with special care to avoid unnecessary increases in required design parameters.

The concept selection process showed that the configuration with aft-mounted engines was capable of having more laminar flow due to the absence of components that could affect the wing laminarization. That reduced the amount of power battery required, which affected aircraft weights and reduced overall DOC. On the other hand, balancing the configuration with aft-mounted engines was more difficult than the conventional configuration. Moreover, the field performance of the conventional configuration was superior to the one with aft-mounted engines. However, differences in the battery and overall weights were significant to select the aft-mounted configuration.

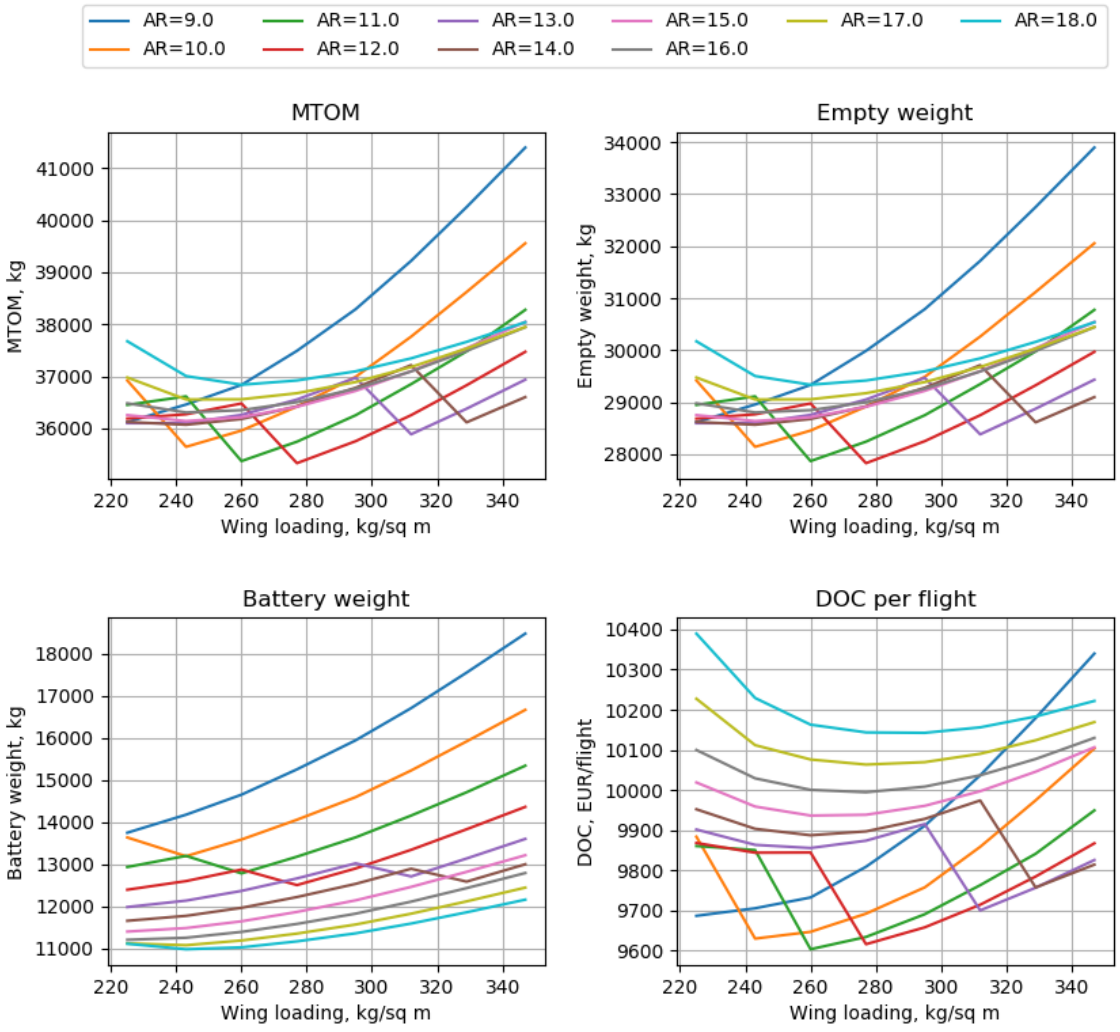

Fig. 5 Summary of the aspect ratio and wing loading trade studies for the short-range all-electric aircraft.

Aircraft refinement using MDO was performed using coupling with MATLAB Genetic Algorithm and SUAVE

mission analysis. Multiple objective functions were considered for the optimization. Table 3 summarizes the optimization problem. Cases for the minimization of DOC and battery weight were considered to investigate relationships between the emission level and DOC and how aircraft configurations may change with changes in objective functions.

Table 3 SE^{2}A SR aircraft optimization problems definition

		Lower	Upper	Units
minimize	1. DOC			
	2. W_b			
wrt	AR	8.00	16.00	
	λ	0.25	0.75	
	C_r	3.00	7.00	m
	$t/c\|_{root}$	12.00	18.00	%
	$t/c\|_{tip}$	12.00	18.00	%
	P/W	0.05	0.30	
subject to	Take-off field length (TOFL)		1400.0	m
	$P/W - P/W\|_{climb}$	0.0		
	Landing field length (LFL)		1100.0	m
	η_{max}		1.0	
	b		50.0	m
	C_t		1.4	m

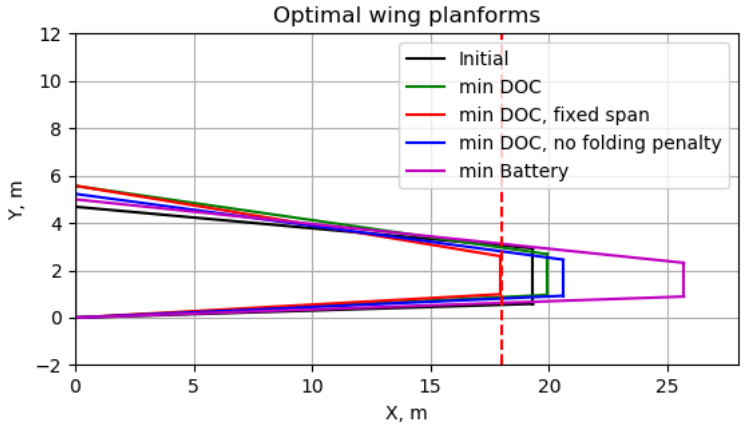

Fig. 6 Wing planforms comparison for different optimization problems.

Fig. 6 shows results for various optimization cases: a case with DOC minimization objective, a similar case with the fixed span constraint of 36m, a case to minimize DOC without the wing folding penalty (as an example to quantify the wing folding penalty sensitivity), and the case of the minimum battery weight. The comparison of different optimizations shown in Table 4 suggested that DOC plays an important role in aircraft feasibility, and its values are substantially larger than the reference aircraft. In addition, the DOC-optimal solution shows a minor increase in the wingspan compared to the Class-C airport regulations. Consequently, to reduce the design complexity associated with the wing folding mechanism, the configuration corresponding to the minimum DOC and the span of 36m was chosen.

In addition, a set of sensitivity analyses using were performed to investigate how airframe technologies and battery energy densities affect the all-electric aircraft feasibility. In addition, the sensitivities of DOC to the maintenance cost penalty factor were considered. Results presented in Fig. 7 show that airframe technologies are able to reduce the aircraft Maximum Take-off Weight (MTOW) substantially compared to the case when no airframe technologies are used. In addition, the aircraft with airframe technologies reduces the required battery weight and equivalent emission level. It

Table 4 Comparison between optimized concepts.

Parameter	Initial design	DOC-optimal design	DOC-optimal design (no folding)	DOC-optimal design (no folding)	Battery-optimal design	ATR-72	Units
W_0	35369	34441	33649	34783	35745	23000	kg
W_e	27869	26941	26149	27283	28244	13311	kg
W_b	12783	12262	11527	10379	13861	-	kg
AR	11.0	10.86	12.23	16.0	10.0	12.0	-
b	38.7	39.6	41.3	51.7	36.0	27.05	m
λ	0.5	0.31	0.3	0.285	0.29	0.55	-
S_{wing}	136.0	145.4	139.6	165.5	129.3	61.0	sq m
$t/c\|_{root}$	0.18	0.18	0.18	0.17	0.18	0.18	-
$t/c\|_{tip}$	0.13	0.13	0.13	0.12	0.12	0.13	-
P/W	0.143	0.125	0.13	0.11	0.14	0.16	kW/kg
DOC	9603	9479	9397	9838	9573	6740	EUR/flight
m_{CO_2}	2045	1961	1844	1660	2217	11838	kg
TOFL	1338	1381	1368	1360	1392	1367	m
LFL	1025	972	985	934	1027	1207	m

also enables lower DOC values until 980 Wh/kg compared to the aircraft without airframe technologies. However, if battery energy density increases more than maintenance and capital costs become of a similar order of magnitude, giving the aircraft without technologies an advantage in DOC. If the sensitivity of DOC to the maintenance cost gain factor is considered, the DOC value does not approach the reference ATR-72 value rapidly. The only option to have a similar DOC value may happen if airframe technologies do not have maintenance cost penalties and feature relatively large battery energy density.

A more detailed description of the design procedure, formulations used, and research outcomes are found in Ref. [25].

2. Initial sizing of the SE^{2}A Mid-range aircraft

A similar initial design to the short-range aircraft was performed for the mid-range aircraft. Design goals included the investigation of effects of airframe and propulsion technologies on the emission of a kerosene-based aircraft, applicability of the hybrid-electric version of this aircraft with the presence of future technologies, and sensitivities of overall aircraft emissions on technology deviations. TLRs were selected similar to the reference A320 and are summarized in Table 5. Similar airframe technologies as for the short-range aircraft were considered. In addition, high bypass ratio turbofan engines with boundary layer ingestion were considered. Two engines are located above the wing to mitigate the noise, and one engine is located at the fuselage to maximize BLI benefits. Two configurations shown in Fig. 8 were considered: the forward- and backward-swept aircraft. Both wing configurations have constraints of the leading edge sweep of 17 degrees to ensure natural laminar flow (NLF) on the front part of the wing while the suction is applied in the middle of the wing. Based on the findings of Sudhi [36], the boundary layer transition was assumed at 65% for both airfoil sides. DLR F15 airfoils were selected for the initial design. The wing thickness at the root and tip were equal to 13.5% and 11% respectively, similar to the aerodynamic design reported in [37]. The wing thickness distribution was selected similar to the A320 to avoid potential early design issues related to low thickness and insufficient space for the landing gear. Regarding the wingspan, to satisfy Class-C airport regulations, the SE^{2}A aircraft wing must be foldable, so the span of the flaps is limited by the folding rib location. The initial designs also used single-slotted Fowler flaps and no leading-edge devices to enable natural laminar flow capabilities. Landing gear positioning was considered differently for both forward- and backward-swept configurations. The backward-swept configuration cannot utilize the conventional landing gear location due to the engine locations and the shift in the empty weight CG. So, similar to the aircraft described in [38], the landing gear was added inside the pylons under the wing-mounted engines. However, similar to [39] an additional drag penalty of 15% was added to the backward-swept

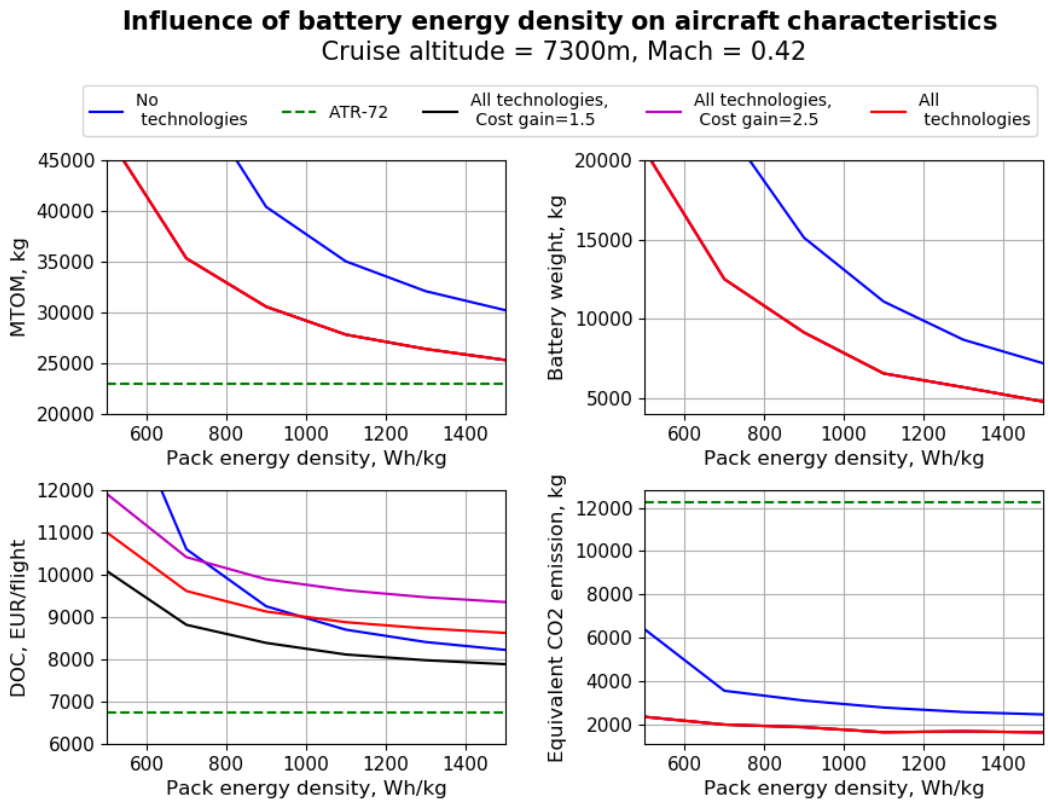

Fig. 7 Summary of influence of battery energy density and aircraft manufacturing cost penalties on the aircraft characteristics.

Table 5 SE^{2}A Mid-range aircraft Top-level Requirements

Parameter	Value	Units
Design range for maximum payload	3981	km
Maximum number of passengers	186	
Maximum payload weight	19625	kg
Cruise Mach number	0.78	
Climb rate at Top-of-Climb	3.00	m/s
Sustained turn angle at the cruise altitude	15	deg
Range with maximum payload	3982	km
Take-off field length	2000	m
Landing field length	1530	m
Certification	CS-25	

configuration.

Initial studies considered kerosene-base aircraft. The initial configuration sizing included the constraint analysis and the trade study between the wing loading and aspect ratio. Figs. 9 and 10 show results of the sensitivity analysis for the forward-swept configuration. Presented results show that induced and compressibility drag have a similar order of magnitude, while the parasite drag has the largest impact on the overall drag. However, the combined effect shows that minimum drag is reached at a lower wing loading compared to the reference A320. Consequently, minimum fuel weight is reached at the aspect ratio of 13.5 and the wing loading of 375 kg/m^2. In addition, a discontinuity region

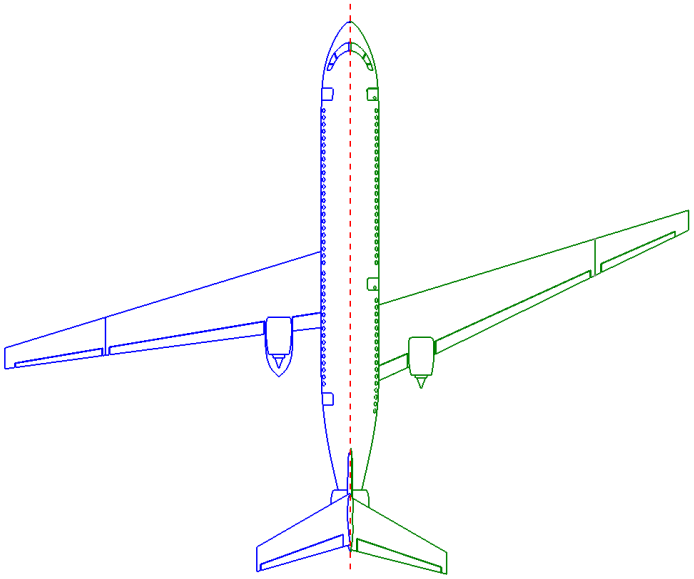

Fig. 8 Configuration layouts for the backward- and forward-swept mid-range aircraft.

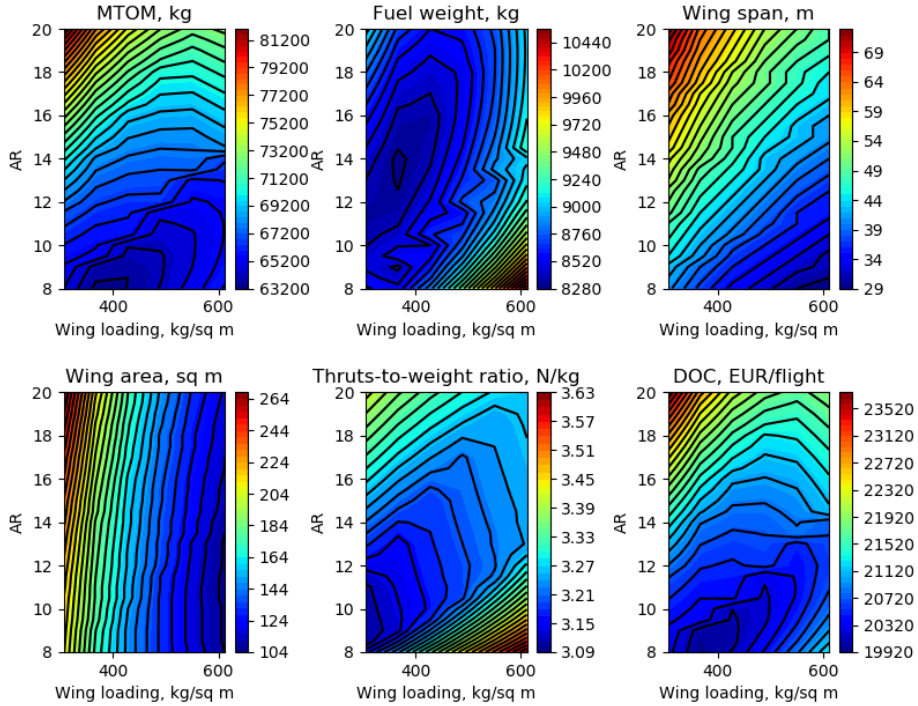

Fig. 9 Summary of the SE^{2}A MR aircraft aspect ratio and wing loading trade studies.

observed in Fig. 9 demonstrates the effect of the wing folding on aircraft weights and DOC. a similar analysis was performed for the backward-swept configuration to obtain initial aircraft specifications. Obtained results of the initial sizing showed that the backward-swept configuration had larger weights compared to the forward-swept configuration. Weight penalties of the backward-swept configuration corresponded to a lower half-chord wing sweep which increased the compressibility drag. In addition, the fuselage laminarization ratio was lower for the backward-swept configuration due to the wing root position with respect to the fuselage. Finally, additional drag penalties due to wing-mounted pylons embedding the landing gear introduced an additional drag component. Consequently, the aerodynamic efficiency of the

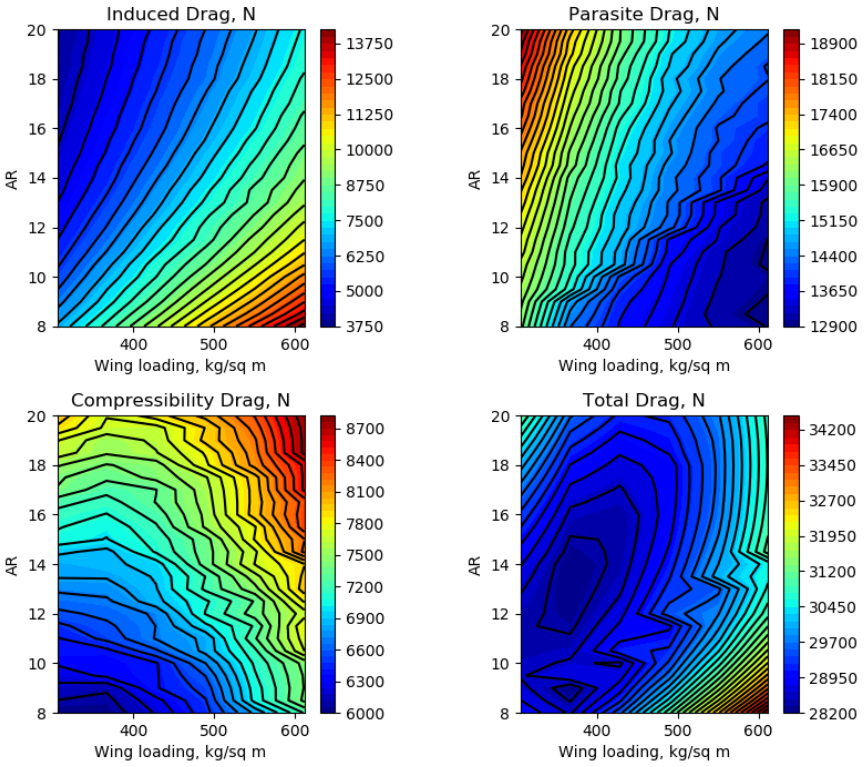

Fig. 10 SE^{2}A MR drag break-down for aspect ratio and wing loading trade studies.

backward-swept configuration was reduced compared to the forward-swept one and lead to higher fuel burn.

After the configuration selection and initial sizing processes, the question of technology sensitivity was assessed. It is generally important to know what technologies influence aircraft sustainability and how sensitive the overall emission is to deviations from desired technological advancements. For the sensitivity analysis, HLFC bounds between 0% and 70%, limit load factors between 2.0 and 2.5, and structural weight reduction between 0% and 20% were considered. BLI and UHBPR engines were considered as total propulsion technology and were assumed either present or absent. The sensitivity analysis summary is shown in Fig. 11.

Comparing cases without influences of engine-related technologies, multiple trends are observed. First, For any level of load alleviation and airframe weight reduction, the emission level achieves higher values than the reference if no HLFC or low level of HLFC is achieved. Such behavior is related to the configuration, which has a higher fuselage and propulsion system weight due to the aft-mounted engine. Reducing the limit load and airframe weight to maximum considered values does not lead to sufficient improvements in the emission level due to a higher default weight in the case of no technologies. Consequently, this configuration is inapplicable without HLFC if engine technologies are absent and a conventional configuration is recommended. The load alleviation technology shows the smallest influence on the emission level since it is applied only to the wing. The strongest influence is observed by the HLFC. By having at least 25-30% laminar flow, minor emission reduction is achievable. While the fuselage will have to use suction, the wing may even achieve such values with NLF [36] which, if sufficient surface treatment is done, will significantly simplify the wing structural design. If all airframe technologies are applied, then the maximum equivalent CO_2 reduction may reach 15%.

If engine technologies are included, similar airframe sensitivity trades are observed, but UHBPR engines and BLI significantly improve the emission level. If not airframe technologies are used, the emission level can be reduced by 13% by improving engines and introducing the BLI. It is important to note that most SFC benefits come from the UHBPR engines, so if such engines are introduced, the emission level will reduce significantly. The emission reduction is improved even further if the aircraft can be laminarized. Finally, among all technologies considered, engine technologies play the most important role in achieving more sustainable aircraft. The second important technology is the HLFC which is followed by airframe materials and structure concepts. Finally, the least impact is achieved by the

load alleviation.

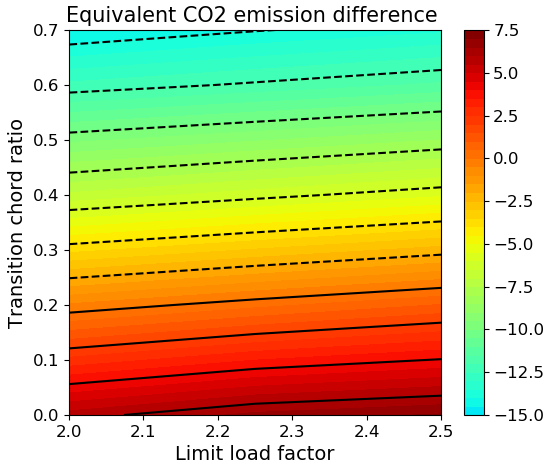

(a) Airframe weight reduction = 0%, no BLI and UHBPR engines

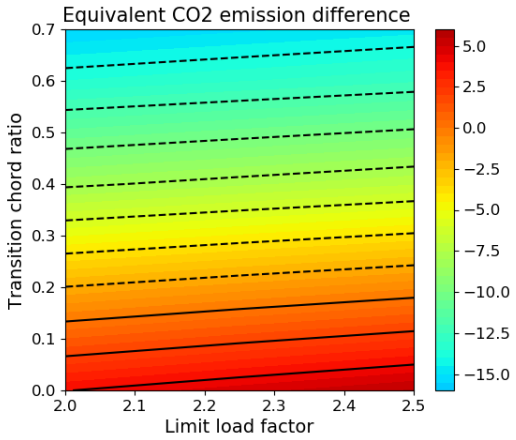

(b) Airframe weight reduction = 10%, no BLI and UHBPR engines

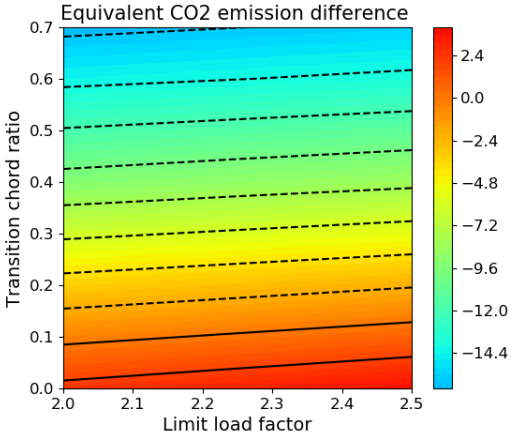

(c) Airframe weight reduction = 19%, no BLI and UHBPR engines

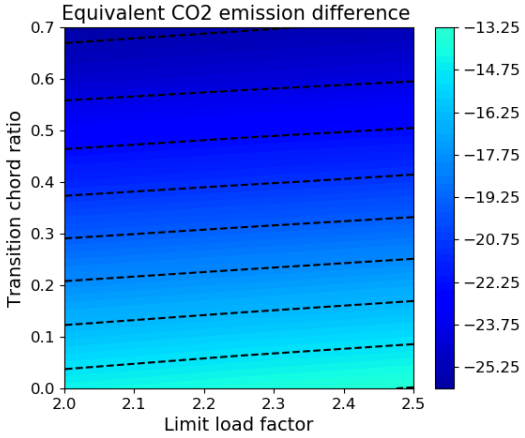

(d) Airframe weight reduction = 0%, BLI and UHBPR engines

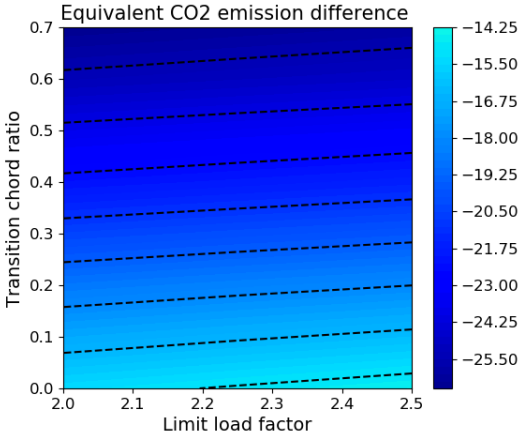

(e) Airframe weight reduction = 10%, no BLI and UHBPR engines

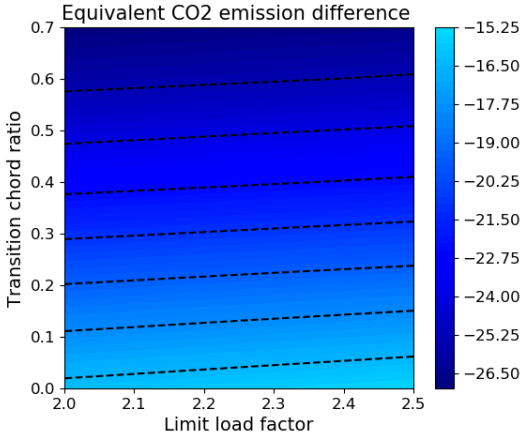

(f) Airframe weight reduction = 19%, no BLI and UHBPR engines

Fig. 11 Equivalent CO_2 emission comparison between the Se^{2}A MR and A320-200 aircraft

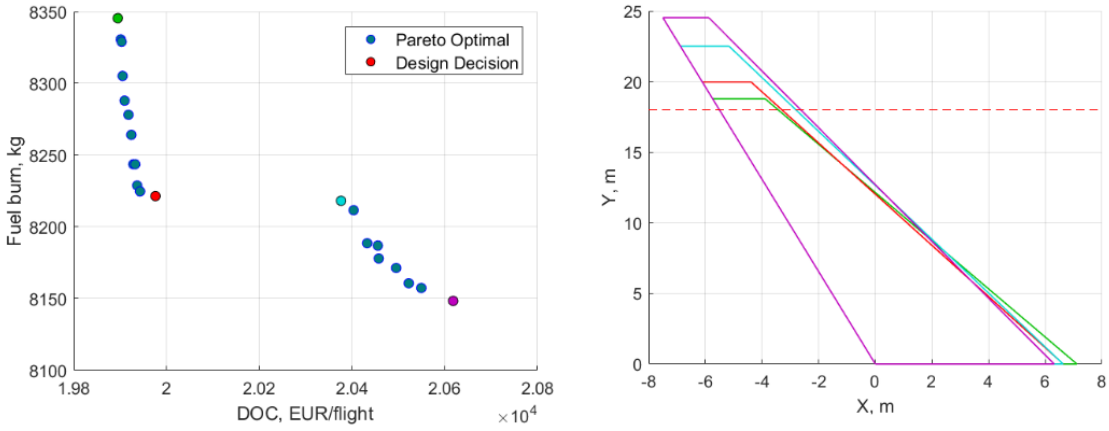

Fig. 12 Pareto from and corresponding wing planforms for selected design cases.

After the initial sizing and sensitivity analyses, the multi-objective optimization of the forward-swept configuration was performed to investigate the relationship between the aircraft DOC and its fuel burn, which is directly proportional to the aircraft CO_2 emission level. the MATLAB GA algorithm was used to perform the aircraft optimization. Table 6 shows the optimization problem. design variables include wing geometric properties and the aircraft thrust-to-weight ratio, while constraints are set based on Top-level Requirements. Final optimization results and wing planforms that correspond to the selected design point on the Pareto front are shown in Figs. 12 and 13.

Table 6 SE^{2}A MR aircraft optimization problem definition

		Lower	Upper	Units
minimize	1. W_f			
	2. W_f, DOC			
wrt	AR	11.00	19.00	
	λ	0.25	1.00	
	C_r	2.00	9.00	m
	$t/c\|_{root}$	13.00	15.00	%
	$t/c\|_{tip}$	10.00	12.00	%
	T/W	0.10	0.50	
subject to	$T/W - T/W\|_{take-off}$	0.0		
	$T/W - T/W\|_{cruise}$	0.0		
	$T/W - T/W\|_{turn}$	0.0		
	$T/W - T/W\|_{climb}$	0.0		
	$W/S - W/S\|_{landing}$		0.0	
	η_{max}		1.0	
	b		55.0	m
	C_t		1.35	m
	$DOC - DOC_{A320}$		0.0	

Results of the multi-fidelity optimization demonstrated two main trends. First, the Pareto front features a discontinuity related to the definition of the wing folding penalty. Moreover, the aircraft is more sensitive to DOC than fuel burn, so it is possible to select the point of minimum DOC and minor changes in the fuel burn. The red point shown in Fig. 13 was selected as the final design configuration for the kerosene-based aircraft.

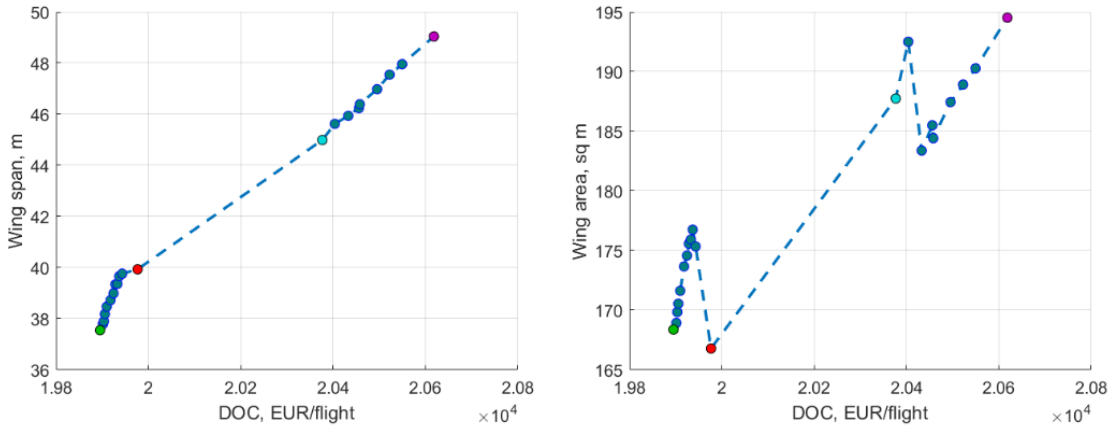

Fig. 13 Aspect ratio and wing spans for selected Pareto-optimal cases.

The analysis of a parallel hybrid-electric version of the aircraft has not shown any benefits in fuel burn for the optimistic case of the battery energy density of 1000 Wh/kg. For the given energy density, the aircraft can have the fuel burn reduction only until the range of 1570 km. Longer ranges make the aircraft heavier even for a small level of aircraft hybridization and do not make the hybrid-electric aircraft feasible.

Finally, a preliminary version of the kerosene-based design was transferred into the internally-developed flight simulator to assess static and dynamic stability deeper. Before the analysis, the simulator performance was validated based on existing data of DC-8-10 and demonstrated sufficient accuracy to be used [40]. The Se^{2}A aircraft was analyzed using the flight simulator and compared against stability characteristics of the Convair CV-880M, since this aircraft was the closest one to the designed aircraft with available stability characteristics information in the literature. Although it was proven to be stable and satisfied flying qualities requirements, it was recommended to increase the wing dihedral angle and the empennage to achieve better stability characteristics

B. Short-range and mid-range aircraft medium-fidelity MDO

The section involves the short and medium range SE^{2}A aircraft analysis considering the development of a MDO framework inside a medium fidelity level.

1. Short-range medium-fidelity MDO

The SE^{2}A short-range aircraft is optimized according to a medium-fidelity level, including boundary layer suction, load alleviation and the use of novel materials, and electric propulsion [41]. Laminar flow control is equipped for the upper lifting surfaces and full fuselage, for laminar flow until wing junction. The attention is mainly focused on developing a framework able to simulate HLFC inside a quasi-three-dimensional analysis coupled with a weight estimation tool. In particular, low fidelity data are used as input of the optimization. Some pre-calculations are done to initiate the MDO process. The initial wing weight W_w is given by EMWET [23] using the aerodynamic loads obtained by Q3D [11]. The rest weight W_{rest} is obtained considering the wing weight computed by EMWET, battery weight, and by subtracting them from the total aircraft gross weight from conceptual design. W_w takes into account the use of load alleviation by reducing the aircraft limit load factor from the required 2.5 to 2.0. Besides, a wing weight reduction of the 15% is applied due to the use of novel materials. The XFOILSUC tool [29–31] is integrated with Q3D to provide accurate drag estimation considering BLS. The strategy implemented is to have natural laminar flow at the forepart of the airfoil and then the application of boundary layer suction to extend the laminar region. Suction is applied on the upper surface only. The desired laminar portion represents the 80% of the chord. D_{rest} represents the drag given by the aircraft without considering the wing, it is computed from C_{Drest}, as the difference between $C_{Dcruise}$, given by the low fidelity $(L/D)_{cruise}$, and the wing drag coefficient C_{Dstart} running Q3D in viscous mode. D_{rest} and W_{rest} are fixed because the wing only is involved in the optimization. Range represents a top-level requirement, given by the Breguet formula, modified for electric propulsion [42]:

$$R = E^* \cdot \eta_{total} \cdot \frac{1}{g} \frac{L}{D} \frac{m_{battery}}{m} \tag{1}$$

The formula is characterized by the product of the battery actual energy density E^*, the total efficiency of the electric propulsive system (η_{total}), average lift to drag ratio for cruise mission ($\frac{L}{D}$) and finally the ratio between battery mass to total mass ($\frac{m_{battery}}{m}$). The performance module involves the use of Eq. (1) for the battery mass estimation. The extended design structure matrix (XDSM) of the optimization problem is shown in Fig. 14[41].

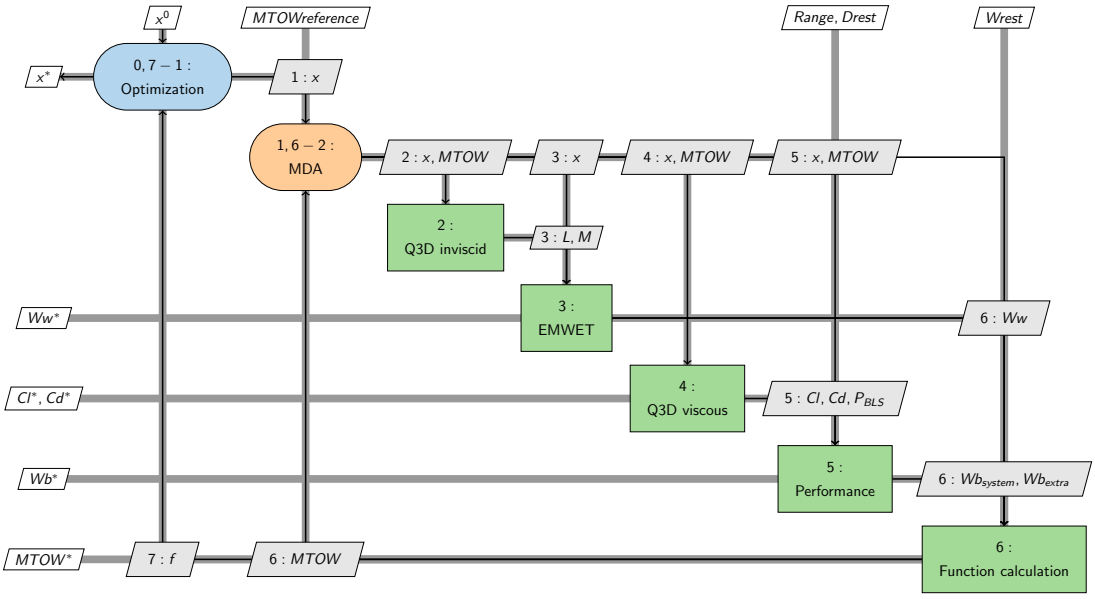

Fig. 14 XDSM for short-range wing optimization framework [41].

The aircraft maximum take-off weight is used as the objective function. Two different configurations are analyzed, the first equipped with the NACA 65(2)415 airfoil and the second with the HLFC SE^{2}A airfoil [36]. The shapes are fixed while the maximum thickness to chord ratio at root and tip represent design variables. Besides, the geometry is optimized, allowing the variation of span, leading-edge sweep angle, chord root, and taper ratio. A gradient-free optimization algorithm is used. The use of XFOILSUC in a gradient-based optimization is discouraged because of the lack of derivatives computation and the possibility of convergence issues that would affect the gradient. Considering the current cases (low speed, regional electric aircraft), the take-off, landing, and climb performance are considered by keeping the wing loading smaller or equal to that of the reference aircraft. No constraint is necessary for the aspect ratio, considering the high initial value (>8). The framework has been applied in [41], results show more than 5% of MTOW reduction and the extra mass necessary due to the power absorption of the boundary layer suction is less than 2% of the battery mass necessary for the mission. Final airfoils are presented in Fig. 15. Profile drag is reduced by the active flow control while induced drag by the increment of the span Fig. 16. The potential augmentation of the surface is compensated by the aerodynamics benefits.

The effect on drag reduction using BLS on the optimized configurations is proofed in Table 7. Further details, including reference and optimized results, can be found in [41].

Table 7 BLS reductions [41]

Wings	$C_{D profile}$	$C_{D wing}$	$C_{D aircraft}$
NACA 65(2)415	-38.73%	-18.56%	-45.84%
SE^2A	-36.62%	-16.12%	-45.50%

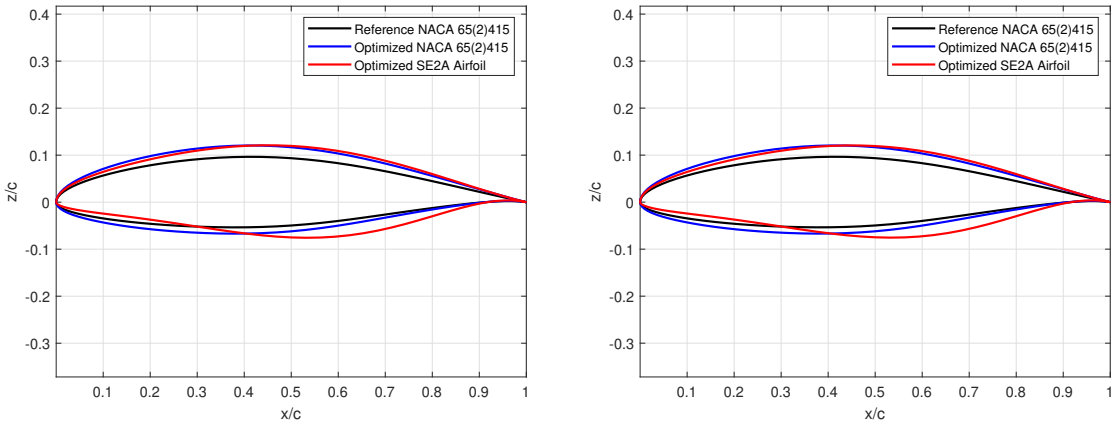

(a) Root comparison. (b) Tip comparison.

Fig. 15 Comparison of NACA 65(2)415 and SE^2A airfoil at root and tip, respect the reference one [41].

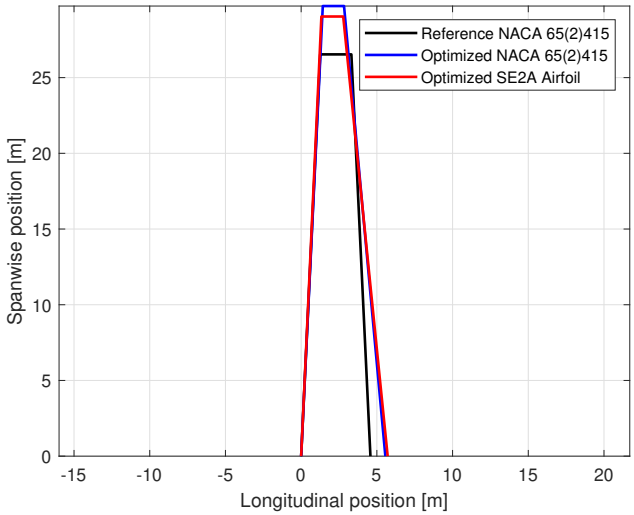

Fig. 16 Wing geometry comparison [41].

2. Mid-range medium-fidelity MDO

A medium-fidelity but physics-based analysis is performed to investigate the advantages of the mentioned novel technologies on the preliminary SE^{2}A mid-range aircraft. The framework intends to obtain accurate results keeping low the computational power. For this purpose, the coupled-adjoint aerostructural analysis and optimization tool FEMWET [32] is modified to consider the effect of active flow control and active load alleviation on the outcome of a wing aerostructural optimization and, consequently, on the overall aircraft fuel efficiency. FEMWET consists of a quasi-three-dimensional aerodynamic analysis and a finite beam element structural solver coupled with the Newton method. The aerodynamics module presents a Vortex Lattice Method (VLM) to compute aerodynamic loads like lift and pitching moment and the induced drag, while viscous and wave drag evaluation is performed by a viscous 2D airfoil analysis. This approach combines the conventional low computational cost of a 2D analysis but with the accuracy of higher fidelity models. In particular, the structure takes into account the effect of sweep angle and taper ratio for each station of the wing and the consequent total parasite drag given by the strip theory. The software MSES [13] is used for the estimation of viscous drag. MSES is an interactive viscous/inviscid Euler method, the software aids in the analysis and design for single and multi-element airfoils at low Reynolds numbers and transonic Mach numbers. In addition, it can predict local flow features such as boundary layer separation and transition, investigate effects of geometry changes [43]. Three general sources of instabilities may occur on the wing during flight: Tollmien – Schlichting instabilities (TSI), cross-flow instabilities (CFI), and attachment line transition. The transition from laminar to turbulent flow is due

to the amplification of these instabilities. Boundary layer suction is an approach towards dampening the growth of these instabilities. In particular, the transition to turbulent flow is delayed by removing a small portion of the boundary layer near the wall. Active flow control technology implies the use of Boundary Layer Suction (BLS) for friction drag reduction. The technology is simulated by individually correcting different drag components that are found to be influenced by BLS, such as friction and pressure drag, without acting on the portion related to the wave drag. A campaign of 2D airfoil simulations at different flight conditions is performed to predict the correction coefficients representing these fractions of drag for a transition at various locations of the chord. Considering the impossibility of modifying the boundary layer equations through an approach similar to the work of [29], due to license limitations, a simplified approach is chosen to consider the effect of boundary layer suction on the wing drag. In this approach, the aerodynamic model explained has been modified to take into account drag penalties for different drag components. In fact, MSES runs with the transition of the upper and lower airfoil surface fixed at 3% of the chord simulating full turbulent flow over the airfoil. Then, proper coefficients are applied to reflect the drag reduction because of the active flow control technology. In particular, four different penalties are studied: K_f, K_{p-w}, K_w, K_i, to reduce respectively friction, form (pressure with no wave drag contribution), wave, and induced drag. Hence, the drag coefficient C_D is defined as:

$$C_D = K_f C_{D_{\mathrm{f}}} + K_{p-w} C_{D_{\mathrm{p\text{-}w}}} + K_w C_{D_{\mathrm{w}}} + K_i C_{D_{\mathrm{i}}} \tag{2}$$

A campaign of simulation using MSES has been performed to identify proper values for the correction factors in Eq. (2). Different supercritical airfoils such as DLR F15 and RAE2822 have been analyzed for an average Cl of 0.4 at different Mach and Reynolds numbers for a range of (forced) boundary layer transitions. A linear model is implemented to predict drag values of the airfoil experiencing the desired portion of laminar flow. Drag estimation for a mid-range aircraft for different laminar flow conditions has been studied by Beck et al. [44]. The research is used to compare the values obtained by the drag penalties model, more details can be found in [45]. Penalties used for the current study are shown in Table 8.

Table 8 Drag penalties for different laminar flow portion

Coefficient	80% laminar	70% laminar	60% laminar
K_f	33%	40%	50%
K_{p-w}	20%	20%	33%

From a structural point of view, the elastic wing is modeled as a finite beam placed at its elastic axis. The use of a beam model is preferred with respect to a shell one because the possible increment of accuracy, estimated in literature as about 5%, does not compensate for the consequent increase of computational power [46]. The finite beam is characterized by the generation of nodes placed at the shear centers of each section. Besides, these nodes are determined by the structural properties of the wing box sections. The thicknesses of the wing box equivalent panels represent the input of the tool. The element stiffness, mass, and force matrices are computed and built thanks to the consistent shape functions for a 3D Timoshenko beam. Using the calculated stress distribution for each element, two different failure criteria are determined: failure due to material yield and buckling. The aileron effectiveness represents a constraint for the optimization described. It is expressed as the ratio of the elastic to the rigid roll moment of the wing due to an aileron deflection:

$$\eta_a = \frac{L_{\delta elastic}}{L_{\delta rigid}} \tag{3}$$

The aerostructural system is characterized by the following four systems of governing equations:

$$R_1(X, \Gamma, U, \alpha) = AIC(X, U)\Gamma - RHS(X, U, \alpha) = 0 \tag{4}$$

$$R_2(X, \Gamma, U) = K(X)U - F(X, \Gamma) = 0 \tag{5}$$

$$R_3(X, \Gamma) = L(X, \Gamma) - nWdes = 0 \tag{6}$$

$$R_4(X, \Gamma, U, \alpha, \alpha_i) = Cl_{2d}(X, U, \alpha, \alpha_i) - Cl_{\perp}(X, \Gamma) = 0 \tag{7}$$

In particular, the first equation represents the governing equation of the VLM. The second is linked to the structural finite element model. The third one relates the total lift as equal to the designed wing considering a proper design load factor. The last equation indicates that the sectional lift calculated by the drag tool as MSES needs to be equal to the lift evaluated by the VLM. The coupled system is solved using the Newton numerical method. The present iterative method, together with the sensitivity of any function of interest, demands the computation of the partial derivatives, evaluated using a coupled-adjoint method and Automatic Differentiation (AD). This strategy is shown to be also beneficial to compute the required derivatives efficiently for gradient-based optimization. The performance module consists of the mission fuel weight computation through semi-empirical methods, fixing aircraft range, Mach number, altitude, and engine parameters. During the optimization, five different load cases (Table 9) are considered to evaluate failure criteria.

Table 9 SE^{2}A BWD Mid-Range Load cases

Load case	Type	Aircraft weight	H [m]	M	n [g]
1	pull-up	MTOW	7500	0.89	2
2	pull-up	MTOW	0	0.58	2
3	push-over	MTOW	7500	0.89	-1
4	gust	ZFW	7500	0.89	1.3
5	roll	W_{des}	4000	0.82	1
6	cruise	W_{des}	10600	0.78	1

A gradient based optimization is performed to minimize the fuel weight of the SE^{2}A Mid-range aircraft. The multidisciplinary design problem is defined in Eq. (8):

$$\begin{aligned} \text{Minimize} \quad & W_{fuel_s}(X) \\ \text{w.r.t.} \quad & X \\ \text{subject to} \quad & Failure_k \leq 0 \\ & \frac{L_{\delta 0}}{L_\delta} - 1 \leq 0 \\ & \frac{MTOW/S_w}{MTOW_0/S_{w0}} - 1 \leq 0 \\ & \frac{W_{fuel}}{W_{fuel_s}} - 1 = 0 \\ & \frac{MTOW}{MTOW_s} - 1 = 0 \\ & X_{lower} \leq X \leq X_{upper} \end{aligned} \tag{8}$$

The design vector is:

$$X = [t_{ui}, t_{li}, t_{fsi}, t_{rsi}, G_j, C_r, \lambda, b, \gamma, \epsilon_{kink}, \epsilon_{tip}, W_{fuels}, MTOW_s] \tag{9}$$

The first 4 components represent the thicknesses of the upper and lower equivalent panel, thicknesses of the front and rear spar, all defined in different 10 spanwise positions from root to tip, for a total of 40 variables. Airfoil shapes are parametrized using the Chebyshev polynomials, which modes are represented by the G vector. In particular, 10 modes are used for the upper surface and 10 modes for the lower one, for a total of 160 variables considering 8 different sections. The wing geometry is defined by the chord root, taper ratio, span, sweep angle at the leading edge, twist angle at kink and tip. The kink position is fixed at 25% of the span. Finally, two surrogate variables are introduced, fuel weight and maximum take-off weight, used to avoid iterations during aeroelastic analysis. Prior to starting the full aerostructural optimizations, a series of aeroelastic optimization (fixed wing shape and only optimizing structural variables) is executed for different maximum load factor (n_{max}), to initialize the values of the thicknesses of the equivalent panel and the consequent reduction in the wing weight. Hence, depending on the values of n_{max}, a fast gradient-based optimization with only the first 4 components of the design vector X is performed for minimizing W_w. Both the aerostructural and

aeroelastic problems are characterized by several constraints. The first group consists of constraints on the structure failure, including tensile, compressive and buckling failure criteria. The SE^{2}A mid-range aircraft has been studied considering the A320 as a reference. As a first approximation, the minimum elastic derivative of roll moment with respect to the aileron deflection is used as a constraint during the optimization. A value of 3.94 M Nm/rad is used, computed starting from the properties of the fixed-wing and considering aileron effectiveness of 0.5. The present value for the A320 is based on [47]. The wing loading (MTOW/S) represents another constraint in order to satisfy the take-off and landing requirements. The first step is represented by 3 different aeroelastic optimizations for different maximum load factors to minimize wing weight, varying the thicknesses of the wing-box panels. The optimizations, hence, are characterized by only the first 4 design variables of the vector in Eq. (9). These are the inputs of 9 different aerostructural optimizations (3 optimization for each maximum load factor), which objective function is represented by fuel weight and all the characteristics shown in Eq. (8) and Eq. (9). The whole optimizations framework is clarified in Fig.17.

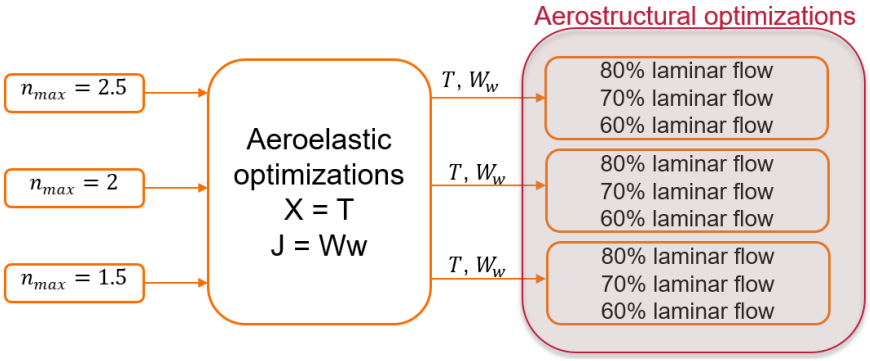

Fig. 17 MDO problem.

Table 10 presents the final results of the optimization. The use of active flow control to achieve 80% laminar flow permits the highest saving of fuel weight. In particular, the reductions are: 7.1%, 7.9%, 8.3% considering respectively n_{max} of 2.5, 2.0, 1.5. The reference is represented by the SE^{2}A mid-range, backward-swept wing with 70% of laminar flow and a maximum load factor of 2.0.

Table 10 Optimizations results

		MTOW [kg]	W_{fuel} [kg]	W_{wing} [kg]	C_L	C_D
Reference		72102	9808	11661	0.397	0.00622
n=2.5	80%	66958	9109	7216	0.393	0.00516
	70%	67172	9204	7335	0.394	0.00548
	60%	67933	9456	7844	0.396	0.00629
n=2	80%	66394	9033	6728	0.379	0.00486
	70%	66313	9117	6563	0.379	0.00524
	60%	66432	9353	6446	0.395	0.00637
n=1.5	80%	65932	8992	6306	0.374	0.00482
	70%	66382	9105	6644	0.377	0.00512
	60%	66590	9354	6602	0.396	0.00633

The optimized geometries for different maximum load factor and considering the variation of laminar flow portion desired, are shown in Fig. 18.

All configurations present a reduction of the sweep angle. The optimizer is looking for wave reduction changing the airfoil shape. A quick look to the percentage reduction of W_f and C_D can be given in Fig. 19, more details about the singular drag components reduced can be found in [45].

For 60% laminar flow, C_D shows minor increment with respect to the reference. In fact, as stated, reference configuration takes into account active flow control for 70% chord. The fuel weight is anyway reduced. In fact, the

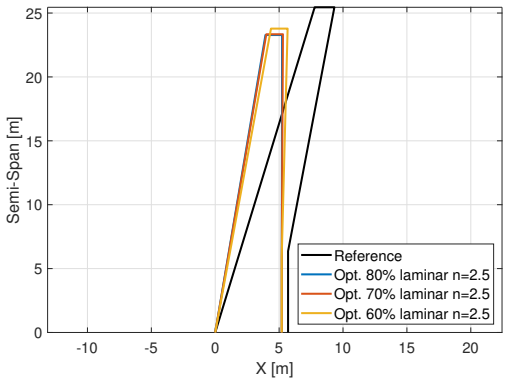

(a) Wing planform n=2.5.

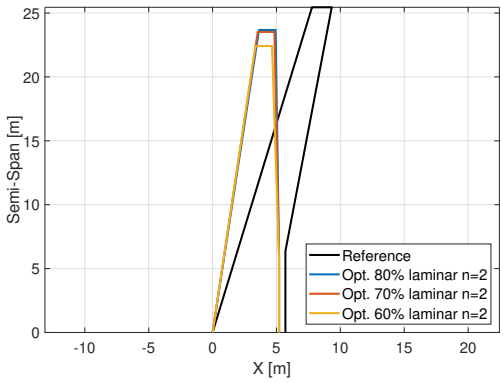

(b) Wing planform n=2.0.

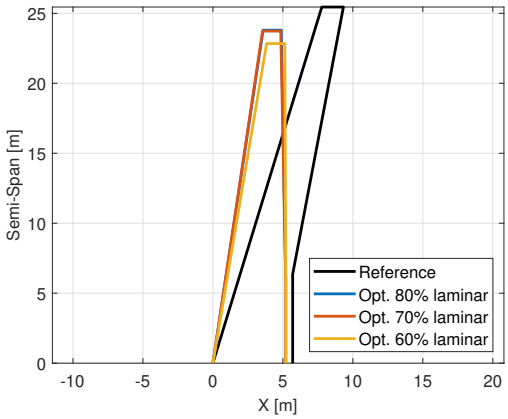

(c) Wing planform n=1.5.

Fig. 18 Wing geometry at different maximum load factor and portion of laminar flow.

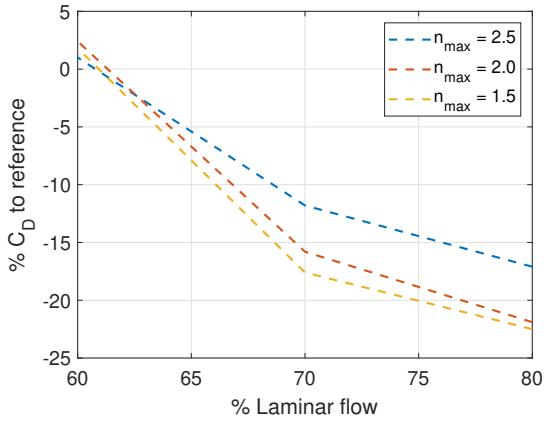

(a) C_D reduction for different n_{max} and laminar flow portion.

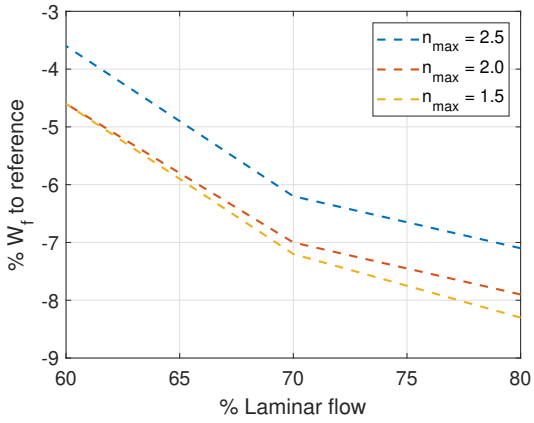

(b) W_f reduction for different n_{max} and laminar flow portion.

Fig. 19 Fuel weight and drag reduction respect to reference, at different conditions.

optimization also acts on the thickness of the wing panels lowering the wing weight and so favoring the objective function minimization. The reference aircraft shows a maximum tip deflection of 2.2 m and a -2.2 deg twist angle for a 1-g cruise mission. The optimized configuration reaches a higher level of flexibility, presenting a bending tip displacement of 2.5-3.2 m and a twist angle between -2.8 deg and -2.6 deg depending on the aerostructural optimization involved. Fig. 20 clarifies the flexibility of the optimized wing, reached with the maximum load alleviation and the same portion of laminar flow of the reference configuration (70% laminar flow). More details, including reference and final results, can be found in [45].

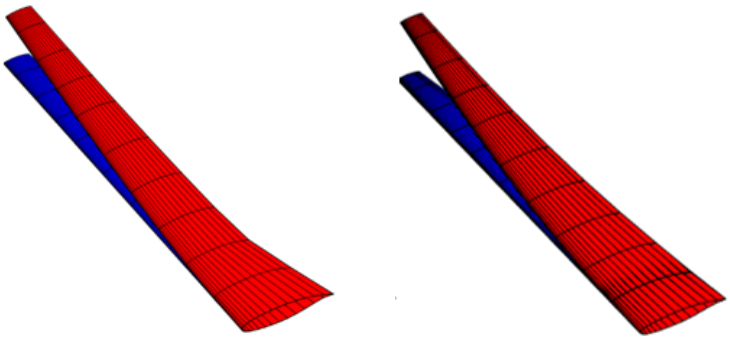

(a) Reference.

(b) Optimized, n_{max} = 1.5, 70% laminar.

Fig. 20 Cruise wing deformation.

C. High-fidelity aerodynamic optimization using ADflow

In this case study, a high-fidelity aerodynamic optimization of two configurations of the mid-range aircraft was performed. Present optimization does not consider any application of active flow control, so a generic comparison of aerodynamic characteristics of each configuration was performed.

To perform the optimization, an open-source CFD code ADflow [48] was used. The Spalart–Allmaras model [49] is adopted as the turbulence model. ADflow also includes an adjoint solver [50], which uses the discrete adjoint implementation via automatic differentiation to compute the derivatives of the functions of interest.

A free-form deformation (FFD) approach was employed to parameterize and manipulate the shape, using the PyGeo [51] - a geometry manipulation module, to parameterize and manipulate the wing shape. In this approach, the surface of the wing was embedded in a grid of control points, and the changes made to the control points were transferred to the embedded surface using a B-spline mapping. When the control points were moved, the embedded shape deformed in a continuous manner, giving the optimizer control over the twist and cross-sectional shapes. To deform the volume mesh during optimization to account for the changes to the surface geometry, the inverse distance weighting method [52] was employed. This mesh deformation was realized in IDWarp [53], an open-source mesh warping module.

Geometric configurations considered for the aerodynamic shape optimization were the forward- and backward-swept versions of the mid-range aircraft without empennages and engine nacelles. Fig. 21 shows CAD-models considered for the study.

The multi-block structured meshes were generated using ICEM CFD software, with 105 blocks. Fig. 22 shows the mesh of BWB configuration, viewed from far-field and near the wall. There were about 50 layers near the configuration to simulate the boundary layer, and the thickness of the first layer was $6.0 \cdot 10^{-5}$ m to obtain y+=10.0. The mesh of forward-swept configuration had the same topology as the backward-swept one. To estimate the accuracy of the numerical methods and verify the mesh convergence, the backward-swept configuration was taken as the example and simulated in the design state under the condition that coefficient of lift C_L=0.4. Four scales of grids were generated, and the numbers of elements in different grids were 660,000 (coarse), 1,600,000 (medium), 3,200,000 (fine), and 6,200,000 (the finest) cells. After the sensitivity analysis, the medium-size mesh was used for the aerodynamic shape optimization.

Free-form deformation (FFD) boxes for both configurations are shown in Fig. 23. Each configuration featured eight spanwise, six chordwise, and two sections along the wing Y-axis. The y coordinates of FFD control points were set to be design variables, making 96 variables. In addition, the twists were also set as design variables, and seven twist variables were set. The angle-of-attack (AoA) was also set as a variable making a total of 104 design variables.

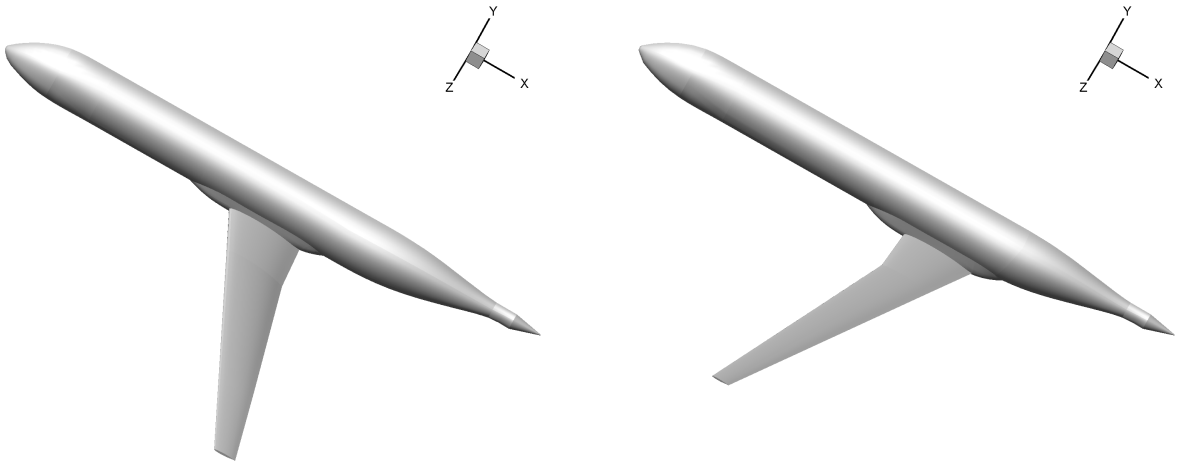

(a) Backward-swept geometry.

(b) Forward-swept geometry.

Fig. 21 Geometric models of SE^{2}A aircraft configurations used for high-fidelity aerodynamic optimization.

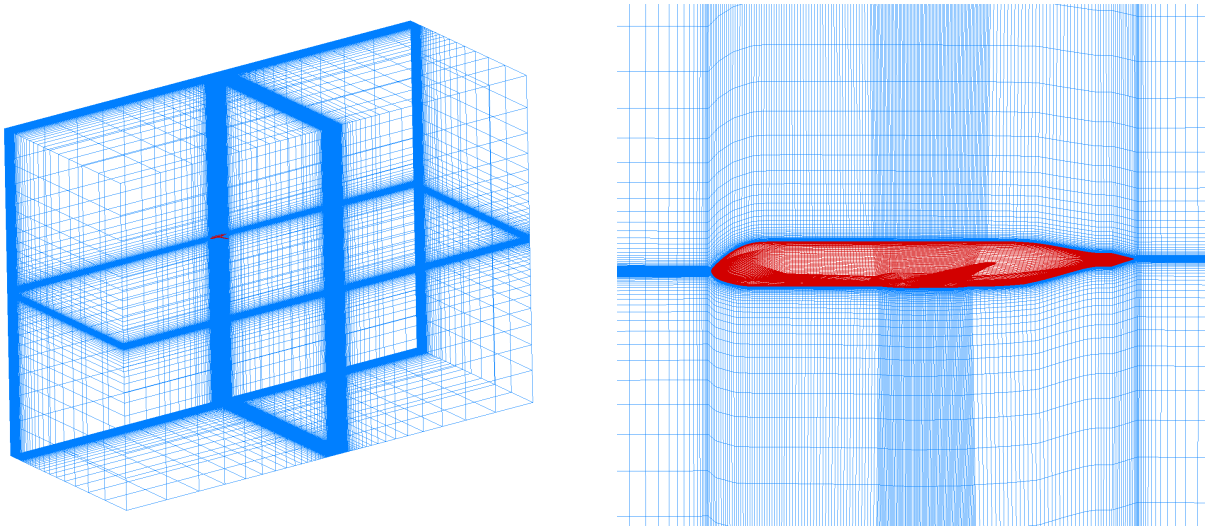

(a) Far-field mesh view.

(b) Near-field mesh view.

Fig. 22 A sample CFD mesh for SE^{2}A aircraft with the backward-swept wing configuration.

Table 11 describes the objective function and constraints of the design problem. The objective function was to minimize the aircraft drag subject to a fixed lift coefficient of 0.4 and having fixed airfoil thickness and internal volume as in the initial aircraft configuration. The optimization method was the sequential least squares programming (SLSQP) algorithm [54].

Figs. 24 and 25 present comparison between initial and final wing shapes using pressure coefficient contours while Table 12 compares optimized forward- and backward-swept models.

Obtained results show that multiple trends. First, both configurations improved their aerodynamic characteristics after the optimization: strengths of sock waves reduced, leading to a reduction in overall drag. Moreover, the forward-swept configuration still outperforms the backward-swept one, although changes have become not substantial.

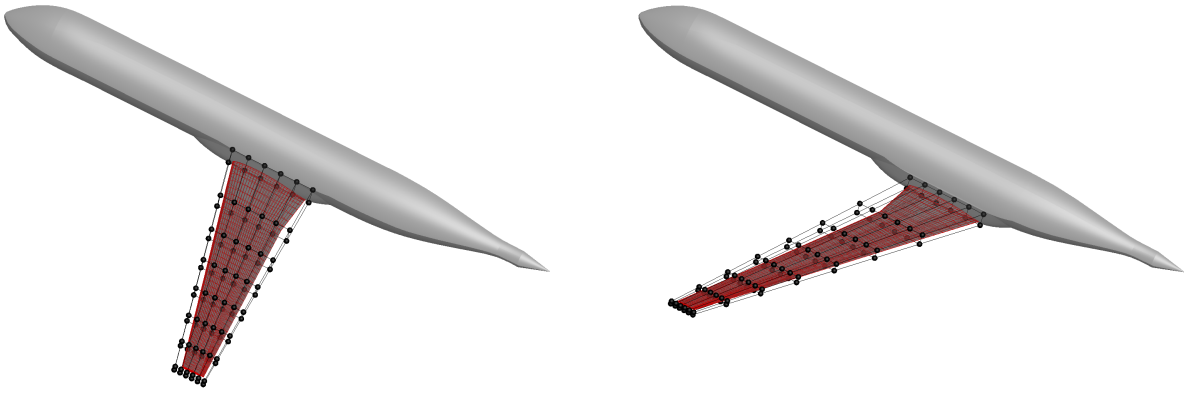

(a) Backward-swept geometry.

(b) Forward-swept geometry.

Fig. 23 FFD box definitions for SE^{2}A aircraft.

Table 11 SE^{2}A LR aircraft aerodynamic shape optimization problem definition

		Lower	Upper
minimize	C_D		
wrt	z		
subject to	C_L	0.4	0.4
	t	t_{base}	t_{base}
	V	V_{base}	V_{base}

Table 12 SE^{2}A MR aircraft optimization summary

Configuration	α	C_L	C_D	L/D
Initial forward-swept	0.084	0.40	0.022	18.16
Initial backward-swept	-1.376	0.40	0.0289	13.85
Optimized forward-swept	-1.043	0.40	0.0207	19.33
Optimized backward-swept	-0.908	0.40	0.0222	18.01

D. Long-range aircraft high-fidelity aerodynamic optimization and low-fidelity analysis

The final case study includes the aerodynamic shape optimization of the long-range blended wing body (BWB) aircraft featuring similar technologies considered for mid-range aircraft. the reference aircraft of B777 and its performance and payload requirements were considered for the aircraft design. Table 13 summarizes the set of TLRs for the long-range aircraft. The initial design of the BWB aircraft is described in [55] and its initial characteristics are shown in Table 14. The aircraft features four CFM 56-7B22 engines that are located at the aft of the BWB such that the BLI capabilities can be utilized. The configuration features winglets for directional control. A model created in OpenVSP is shown in Fig. 26 and its geometric characteristics are summarized in Table 14.

Since SUAVE initial sizing is based on semi-empirical drag estimation methods, it is uncertain if such methods can be successfully applied to the unconventional configuration of the BWB. Consequently, the aerodynamic analysis and aerodynamic shape optimization using SU2 [56] were performed to increase the aerodynamic analysis fidelity and update the SUAVE mission analysis using surrogate models from CFD. The transition between the SUAVE and SU2 was performed using capabilities available within SUAVE and shown in Fig. 27. Based on the figure, an OpenVSP model is

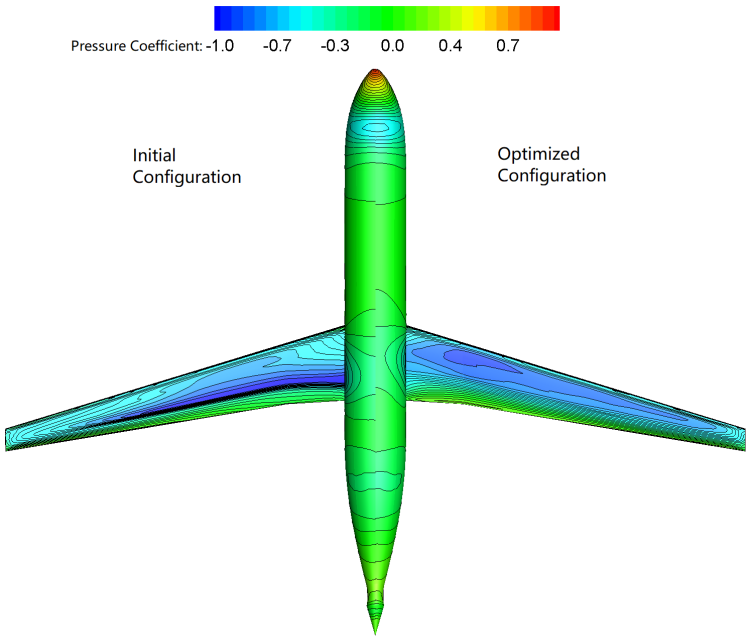

Fig. 24 Pressure coefficient contours for initial and optimized backward-swept configuration.

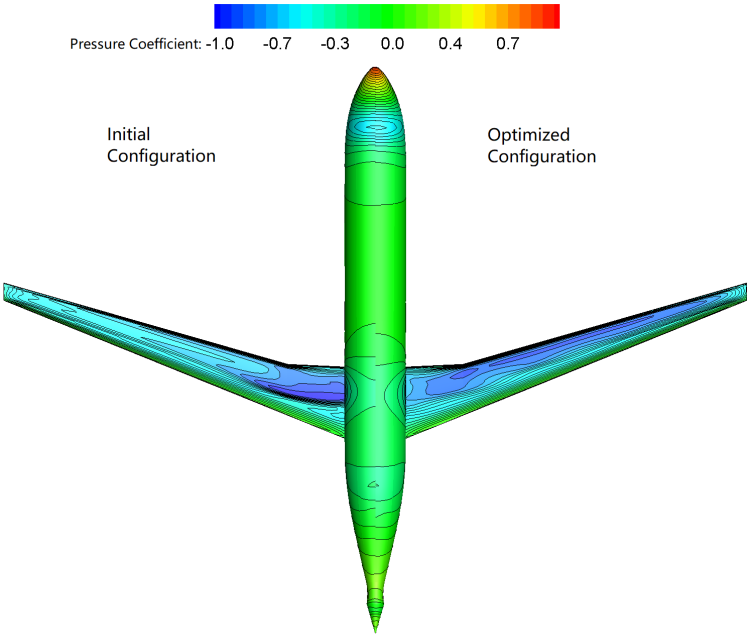

Fig. 25 Pressure coefficient contours for the baseline and optimized forward-swept configuration.

automatically generated using SUAVE geometric characteristics. Then, an unstructured mesh is created in OpenVSP and exported into Gmsh to translate the mesh format to one applicable for SU2. To simplify the analysis and later optimization, the model without winglets was considered for high-fidelity CFD analysis. Fig. 28 shows the geometry considered for the analysis and optimization and a sample CFD-mesh created using OpenVSP. To ensure sufficient resolution of the mesh, a mesh sensitivity analysis was performed. Four meshes were considered: 343612 cells (coarse), 660528 cells (medium), 835000 cells (fine), and 1012683 cells (the finest). The medium-size mesh was selected due to

Table 13 SE^{2}A Long-range aircraft Top-level Requirements

Parameter	Value	Units
Maximum number of passengers	300	
Cruise Mach number	0.85	
Maximum Mach number	0.92	
Design range	15000	km
Take-off field length	2200	m
Landing field length	1966	m
Certification	CS-25	

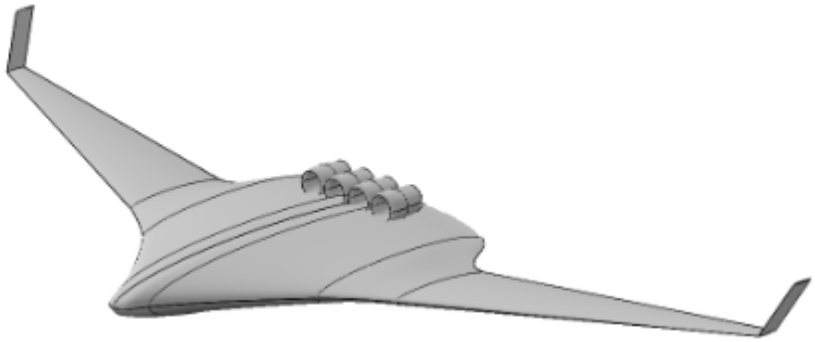

Fig. 26 Geometric layout of the SE^{2}A LR aircraft .

Table 14 SE^{2}A LR aircraft geometric properties

Parameter	Wing	Winglet	Units
b	57.80	3.00	m
AR	7.40	2.00	
λ	0.065	1.00	
C_r	30.60	1.50	m
$\Lambda_{C/4}$	20.00	30.0	deg

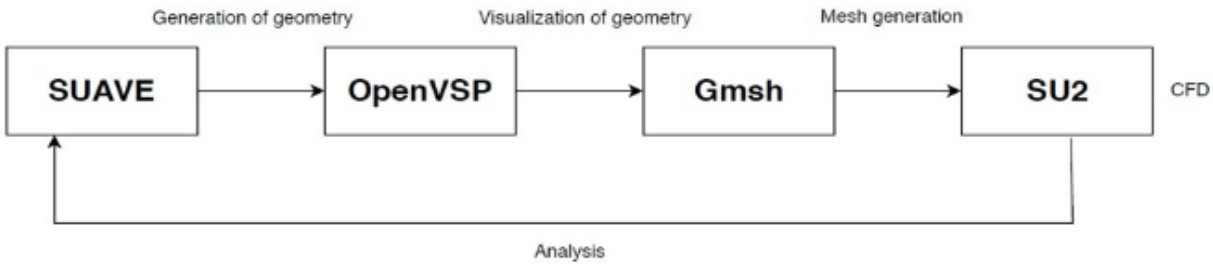

Fig. 27 Sequential build-up from SUAVE geometry to SU2 CFD analysis.

sufficient solution accuracy and reduced computational costs. Finally, SU2 performs required analyses and optimization to return a surrogate model to SUAVE for the new calculation. For the analysis, a CFD solution using Euler equations

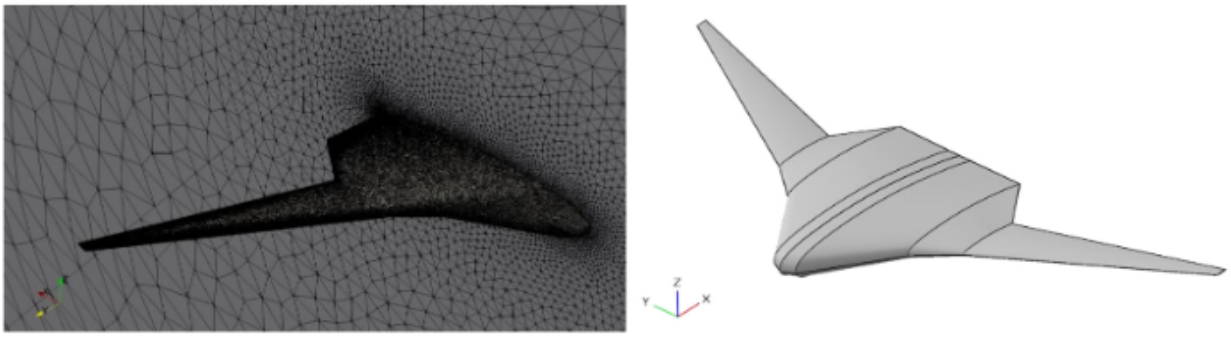

Fig. 28 BWB geometry and its corresponding mesh considered for the aerodynamic analysis using SU2.

was used. From CFD, compressibility drag was extracted to create a surrogate model using the SMT-Toolbox and the RMTB algorithm within it. Other drag components were estimated using semi-empirical formulations.

Fig. 29 shows results for the CFD-analysis of the initial design of the long-range aircraft, and Table 15 shows a comparison between the initially sized aircraft using semi-empirical methods, an updated sizing using the surrogate model, and the reference B777.

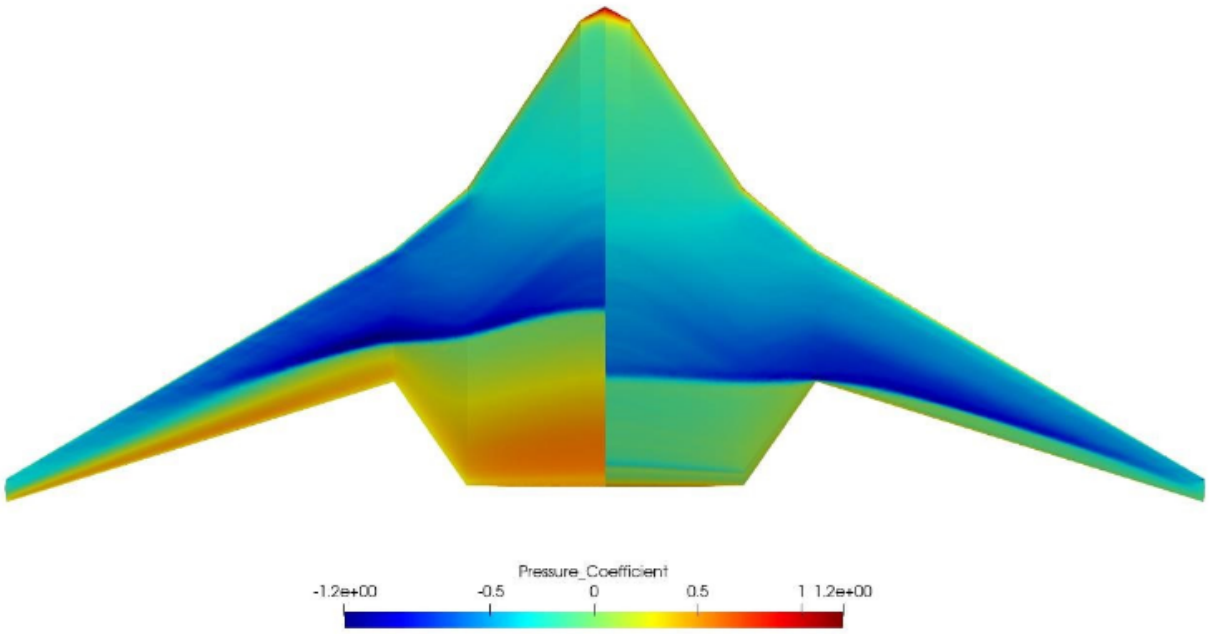

Fig. 29 Pressure coefficient distribution on the pressure (left) and suction (right) sides of the aircraft (α= 0 deg, M= 0.85).

Obtained results show that low-fidelity semi-empirical estimations significantly under-predict potential compressibility drag. When the high-fidelity analysis is used, all significant benefits from novel technologies disappear, and the aircraft fuel efficiency becomes worse than the reference B777.

To improve the aircraft shape and mitigate adverse effects of the compressibility drag, the aerodynamic shape optimization using SU2 was performed. A similar technique using the FFD box was used to discretize the wing. The FFD box with the size of 11x5x2 was created to cover the shape of the aircraft. Fig. 30 shows the FFD box layout and locations of control sections.

Table 16 describes the objective function of the BWB optimization. The goal of the optimization is to minimize aircraft drag at the design lift coefficient of 0.15 and ensure that the control section thickness and leading-edge radii do

Table 15 Comparison of the SE^{2}A Long-range aircraft using semi-empirical and surrogate model drag estimation methods

Parameter	semi-empirical model	Surrogate model	B777	Units
MTOM	255859.0	255859.0	347452.0	kg
OEW	87170.0	87170.0	145150.0	kg
L/D_{max}	48.0	43.0	21.0	-
L/D_{cruise}	34.0	5.0	18.5	-
W_f	28824.0	135681	109290.0	kg
Fuel efficiency	0.64	3.01	2.72	kg/seat/100 km

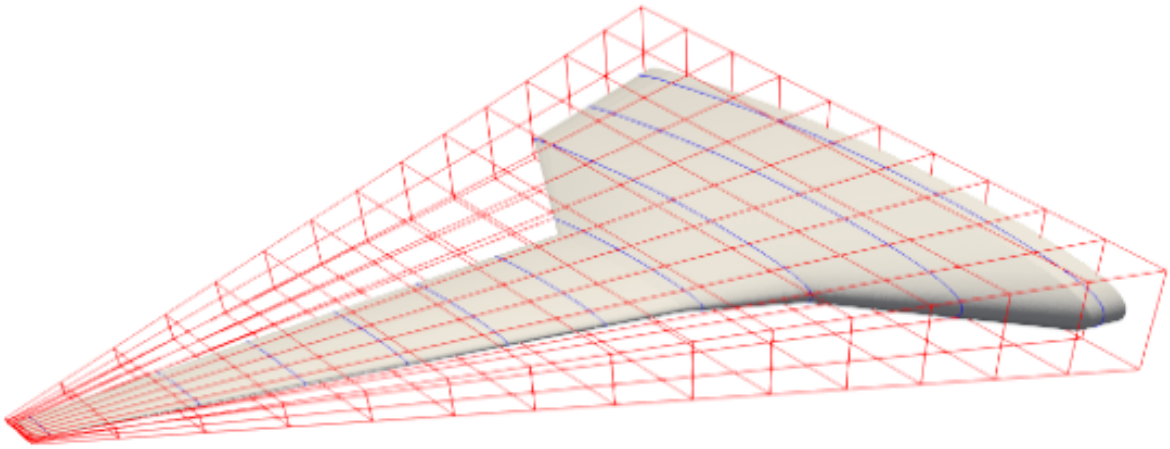

Fig. 30 FFD Box (red) and control sections (blue) of the long-range BWB aircraft.

not reduce by more than 20% to ensure sufficient internal volume and avoid leading-edge separation.

Table 16 SE^{2}A LR aircraft aerodynamic shape optimization problem definition

		Lower	Upper
minimize	C_D		
wrt	z		
subject to	C_L	0.15	0.15
	t/c	$0.8t/c_{base}$	-
	R_{LE}	$0.8R_{LE_{base}}$	-

Fig. 31 shows the suction side pressure coefficient comparison between the initial BWB aerodynamic design and the design after the optimization. Results demonstrate a substantial reduction in inviscid drag coefficient and substantial mitigation of the shock wave.

Finally, angle-of-attach and Mach number sweeps of the optimized BWB aircraft were obtained and exported into SUAVE to estimate its performance again. Table 17 summarizes results of the optimized aircraft SUAVE analysis and compares them against an initial low-fidelity SUAVE simulation and the initial simulation with high-fidelity results. After the optimization, a considerable increase in fuel efficiency was achieved compared to the initial aerodynamic shape. However, high-fidelity effects could not reach fuel efficiency levels similar to the low-fidelity output. Such results suggest using high-fidelity analysis tools as early as possible to avoid potential issues related to simulation fidelity.

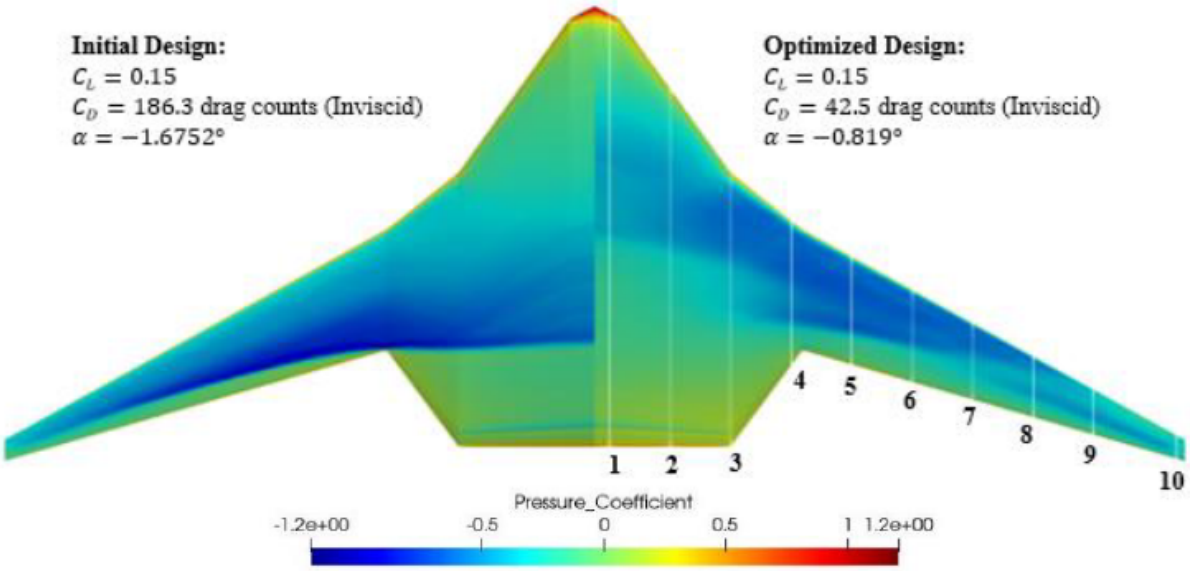

Fig. 31 Pressure coefficient comparison between the initial and optimized BWB configurations.

Table 17 Comparison of the SE^{2}A LR aircraft performance between initial and optimized configurations with respect to relative change from the reference B777

Parameter	Semi-empirical(%)	Initial aircraft surrogate(%)	Optimized aircraft surrogate(%)
MTOM	-58.5	-26.4	-51.1
OEW	-44.2	-39.9	-39.2
L/D_{max}	127.0	104.8	109.5
L/D_{cruise}	83.8	-71.0	21.6
W_f	-73.6	24.1	-55.5
Fuel efficiency	-76.5	10.6	-60.3

V. Conclusion

Present work introduced a multi-fidelity design, analysis, and optimization environment ADEMAO which includes various tools and methods to address the design of future aircraft. Each block is responsible for specific design goals and is connected to other blocks using the universal parametric environment CPACS. The paper described each component of the environment and methods used. In addition, example design, analysis, and optimization cases for aircraft considered under SE^{2}A cluster using ADEMAO was presented to demonstrate the capabilities of the environment.

Four different case studies corresponding to main software capabilities were presented: initial sizing of two reference aircraft, medium-fidelity optimization of reference aircraft wings, high-fidelity aerodynamic optimization of the reference mid-range aircraft wing, and an integration of the initial sizing tool with high-fidelity aerodynamic optimization results of the BWB aircraft. Results demonstrated an unconventional nature of designed aircraft and requirements for a multi-fidelity design approach during the conceptual design.

Acknowledgments

We would like to acknowledge the funding by the Deutsche Forschungsgemeinschaft (DFG, German Research Foundation) under Germany's Excellence Strategy—EXC 2163/1-Sustainable and Energy Efficient Aviation—Project-ID 390881007.

References

[1] *Flightpath 2050-Europe's Vision for Aviation: Advisory Council for Aeronautics Research in Europe*, EUROPEAN COMMISSION: Brussels, Belgium, 2011.

[2] Alder, M., Moerland, E., Jepsen, J., and Nagel, B., "Recent Advances in Establishing a Common Language for Aircraft Design with CPACS," *Aerospace Europe Conference 2020*, 2020.

[3] Lukaczyk, T., Wendroff, A., Colonno, M., Economon, T., Alonso, J., Orra, T., and Ilario, C., "SUAVE: An Open-Source Environment for Multi-Fidelity Conceptual Vehicle Design," *16th AIAA/ISSMO Multidisciplinary Analysis and Optimization Conference*, 22-26 June 2015. https://doi.org/10.2514/6.2015-3087.

[4] Drela, M., and Youungren, H., "Athena Vortex-Lattice Method," 2020. URL http://web.mit.edu/drela/Public/web/avl/.

[5] Gudmundsson, S., *General Aviation Aircraft Design: Applied Methods and Procedures, 1st Edition*, Butterworth-Heinemann, Oxford, UK, 2013.

[6] Howe, D., *Aircraft Conceptual Design Synthesis*, Aerospace Series, Vol. 5, Professional Engineering Publishing Limited, Wiley, 2000.

[7] Mattingly, J. D., *Aircraft Engine Design*, AIAA Education Series, American Institute of Aeronautics and Astronautics, Inc., 1801 Alexander Bell Drive, Reston, VA, USA, 2018.

[8] Scholtz, D., "Aircraft design notes: 5. Preliminary sizing," , 2015.

[9] Bartel, M., and Young, T., "Simplified Thrust and Fuel Consumption Models for Modern Two-Shaft Turbofan Engines," *Journal of Aircraft - J AIRCRAFT*, Vol. 45, 2008, pp. 1450–1456. https://doi.org/10.2514/1.35589.

[10] Nita, M., and Scholtz, D., "Estimating the Oswald Factor from Basic Aircraft Geometrical Parameters," *Deutscher Luft- und Raumfahrtkongress 2012*, 2012.

[11] Elham, A., and van Tooren M., "Quasi-Three-Dimensional Aerodynamic Solver for Multidisciplinary Design Optimization of Lifting Surfaces," *Journal of Aircraft*, Vol. 51, No. 2, 2014. https://doi.org/10.2514/1.C032261.

[12] Drela, M., and Youungren, H., "Xfoil panel method software," 2020. URL https://web.mit.edu/drela/Public/web/xfoil/.

[13] Drela, M., "MSES: Multi-Element airfoil Design/Analysis software, ver. 3.07," 2007.

[14] Torenbeek, E., *Synthesis of Subsonic Airplane Design*, Springer, Netherlands, 1982. https://doi.org/10.1007/978-94-017-3202-4.

[15] Roskam, J., *Airplane design, 2nd Edition*, Darcorporation, 2003, Vol. 1-8.

[16] Hoelzen, J., Liu, Y., Bensmann, B., Winnefeld, C., Elham, A., Friedrichs, J., and Hanke-Rauschenbach, R., "Conceptual Design of Operation Strategies for Hybrid Electric Aircraft," *Energies*, Vol. 11, No. 1, 2018. https://doi.org/10.3390/en11010217.

[17] T., K., Winnefeld.C, R, H.-R., and Krewer, U., "Analysis and Design of Fuel Cell Systems for Aviation," *Enerfies*, Vol. 11, 2018. https://doi.org/10.3390/en11020375.

[18] Kulikovsky, A., "A Physically–Based Analytical Polarization Curve of a PEM Fuel Cell," *J. Electrochem. Soc.*, Vol. 161, No. 3, 2013. https://doi.org/10.1149/2.028403jes.

[19] Nicolay, S., Karpuk, S., Liu, Y., and Elham, A., "Conceptual design and optimization of a general aviation aircraft with fuel cells and hydrogen," *International Journal of Hydrogen Energy*, Vol. 46, No. 64, 2021. https://doi.org/10.1016/j.ijhydene.2021.07.127.

[20] Wells, D., Horvath, B., and McCullers, L., "NASA TM 20170005851," *2018 IEEE International Conference on Electrical Systems for Aircraft, Railway, Ship Propulsion and Road Vehicles International Transportation Electrification Conference (ESARS-ITEC)*, Vol. 1, June 1, 2017.

[21] Verstraete, D., *The Potential of Liquid Hydrogen for long range aircraft propulsion*, Ph.D thesis, Cranfield University, 2009.

[22] Brewer, D., *Hydrogen Aircraft Technology*, 1st ed., CRC Press, Boca Raton, USA, 1991.

[23] Elham, A., La Rocca, G., and van Tooren, M., "Development and implementation of an advanced, design-sensitive method for wing weight estimation," *Aerospace Science and Technology*, Vol. 29, No. 1, 2013, pp. 100–113. https://doi.org/10.1016/j.ast.2013.01.012.

[24] Yarygina, V., M, and Popov, I., Yu, "Development of the Weight Formula for a Folding Wing," *Russian Aeronautics (Iz.VUZ)*, Vol. 55, No. 2, 2012, pp. 120–126.

[25] Karpuk, S., and Elham, A., "Influence of Novel Airframe Technologies on the Feasibility of Fully-Electric Regional Aviation," *Aerospace*, Vol. 8, No. 6, 2021. https://doi.org/10.3390/aerospace8060163.

[26] Dallara, E., *Aircraft Design for Reduced Climate Impact*, Ph.D thesis, Stanford University, 2011.

[27] Scholz, D., "Limits to Principles of Electric Flight," *Deutscher Luft- und Raumfahrtkongress 2019*, 2019.

[28] Bouhlel, M. A., Hwang, J. T., Bartoli, N., Lafage, R., Morlier, J., and Martins, J. R. R. A., "A Python surrogate modeling framework with derivatives," *Advances in Engineering Software*, 2019, p. 102662. https://doi.org/https://doi.org/10.1016/j.advengsoft.2019.03.005.

[29] Ferreira, C., "Implementation of boundary layer suction in xfoil and application of suction powered by solar cells at high performance sailplanes," *Master's Thesis, TU Delft*, 2002.

[30] Bongers, J., "Implementation of a new transition prediction method in xfoil, Predicting transition in suction boundary layers," *Master's Thesis, TU Delft*, 2006.

[31] Broers, R., "Extending XFOIL and xSoaring for Suction-Type Boundary Layer Control Calculations," *Master's Thesis, TU Delft*, 2004.

[32] Elham, A., and van Tooren, M. J., "Tool for preliminary structural sizing, weight estimation, and aeroelastic optimization of lifting surfaces," *Proc IMechE Part G: J Aerosp Eng 230(2):280-295*, 2016. https://doi.org/10.1177/0954410015591045.

[33] "ATR-72 Series 600 Brochure," 2014. URL https://perma.cc/95KA-S7XS.

[34] "Certification Specifications and Acceptable Means of Compliance for Large Aeroplanes CS-25," June, 2020. URL https://www.easa.europa.eu/document-library/certification-specifications/cs-25-amendment-25.

[35] Mconald, A., R, "Advanced Modeling in OpenVSP," *48th AIAA Aerospace Sciences Meeting Including the New Horizons Forum and Aerospace Exposition*, 13-17 June 2016. https://doi.org/0.2514/6.2010-657.

[36] Sudhi, A., Elham, A., and Badrya, C., "Coupled Boundary-Layer Suction and Airfoil Optimization for Hybrid Laminar Flow Control," *AIAA Journal*, 2021. https://doi.org/10.2514/1.J060480.

[37] Seitz, A., Hübner, A., and Risse, K., "The DLR TuLam project: design of a short and medium range transport aircraft with forward swept NLF wing," *CEAS Aeronaut Journal*, , No. 11, 2020, pp. 449 – 459. https://doi.org/10.1007/s13272-019-00421-1.

[38] Giesecke, D., Lehmler, M., Friedrichs, J., Blinstrub, J., Bertsch, L., and Heinze, W., "Evaluation of ultra-high bypass ratio engines for an over-wing aircraft configuration," *Journal of the Global Power and Propulsion Society*, Vol. 2, 2018. https://doi.org/10.22261/JGPPS.8SHP7K.

[39] Savoni, L., and Rudnik, R., "Pylon Design for a Short Range Transport Aircraft with Over-the-Wing Mounted UHBR Engines," *2018 AIAA Aerospace Sciences Meeting*, 8-12 January 2018. https://doi.org/10.2514/6.2018-0011.

[40] Schmidt, L. V., *Introduction to Aircraft Flight Dynamics*, Vol. 1, American Institute of Aeronautics and Astronautics, Inc., 1998.

[41] Mosca, V., Karpuk, S., Sudhi, A., Badrya, C., and Elham, A., "Multidisciplinary design optimisation of a fully electric regional aircraft wing with active flow control technology," *The Aeronautical Journal*, 2021, p. 1–25. https://doi.org/10.1017/aer.2021.101.

[42] Hepperle, M., "Electric Flight - Potential and Limitations," *Potential and Limitations, Energy Efficient Technologies and Concepts of Operation, AVT-209 Workshop on ENERGY EFFICIENT TECHNOLOGIES AND CONCEPTS OPERATION*, 2012.

[43] Drela, M., and Giles, M. B., "Viscous-inviscid analysis of transonic and low Reynolds number airfoils," *AIAA Journal*, Vol. 25, No. 10, 1987, pp. 1347–1355. https://doi.org/10.2514/3.9789.

[44] Beck, N., Landa, T., Seitz, A., Boermans, L., Liu, Y., and Radespiel, R., "Drag reduction by laminar flow control," *Energies*, Vol. 11, No. 1, 2018, pp. 89–127. https://doi.org/10.3390/en11010252.

[45] Mosca, V., and Elham, A., "WING AEROSTRUCTURAL OPTIMIZATION WITH ACTIVE FLOW CONTROL AND ACTIVE LOAD ALLEVIATION," *AeroBest 2021 International Conference on Multidisciplinary Design Optimization of Aerospace Systems*, IDMEC Instituto Superior Técnico Universidade de Lisboa, Lisboa, Portugal, 2021, pp. 616–635.

[46] Dorbath, F., Nagel, B., and Gollnick, V., "Comparison of Beam and Shell Theory for Mass Estimation in Preliminary Wing Design," *RAeS 2nd Aircraft Structural Design Conference*, 2010.

[47] BDM, "Boeing Design Manual BDM 6001," The Boeing Company, Chicago, IL, 1989.

[48] Mader, C. A., Kenway, G. K., Yildirim, A., and Martins, J. R., "ADflow: an open-source computational fluid dynamics solver for aerodynamic and multidisciplinary optimization," *Journal of Aerospace Information Systems*, Vol. 17, No. 9, 2020, pp. 508–527. https://doi.org/10.2514/1.I010796.

[49] Spalart, P., and Allmaras, S., "A one-equation turbulence model for aerodynamic flows," *30th aerospace sciences meeting and exhibit*, 1992, p. 439. https://doi.org/10.2514/6.1992-439.

[50] Kenway, G. K., Mader, C. A., He, P., and Martins, J. R., "Effective adjoint approaches for computational fluid dynamics," *Progress in Aerospace Sciences*, Vol. 110, 2019, p. 100542. https://doi.org/10.1016/j.paerosci.2019.05.002.

[51] Kenway, G. K. W., Kennedy, G. J., and Martins, J. R. R. A., "A CAD-Free Approach to High-Fidelity Aerostructural Optimization," *Proceedings of the 13th AIAA/ISSMO Multidisciplinary Analysis Optimization Conference*, Fort Worth, TX, 2010. https://doi.org/10.2514/6.2010-9231, aIAA 2010-9231.

[52] Luke, E., Collins, E., and Blades, E., "A fast mesh deformation method using explicit interpolation," *Journal of Computational Physics*, Vol. 231, No. 2, 2012, pp. 586–601. https://doi.org/10.1016/j.jcp.2011.09.021.

[53] Secco, N. R., Kenway, G. K., He, P., Mader, C., and Martins, J. R., "Efficient mesh generation and deformation for aerodynamic shape optimization," *AIAA Journal*, Vol. 59, No. 4, 2021, pp. 1151–1168. https://doi.org/10.2514/1.J059491.

[54] Lawson, C. L., and Hanson, R. J., *Solving least squares problems*, SIAM, 1995.

[55] Karpuk, S., Y, L., and Elham, A., "Multi-Fidelity Design Optimization of a Long-Range Blended Wing Body Aircraft with New Airframe Technologies," *Aerospace*, Vol. 7, No. 7, 2020. https://doi.org/10.3390/aerospace7070087.

[56] Palacios, F., Economon, T., Aranake, A., Copeland, S., Lonkar, A., Lukaczyk, T., Manosalvas, D., Naik, K., Padron, S., Tracey, B., Variyar, A., and Alonso, J., "Stanford University Unstructured (SU2): Analysis and Design Technology for Turbulent Flows," *In Proceedings of the 52nd Aerospace Sciences Meeting*, 13-17 January 2018. https://doi.org/10.2514/6.2014-0243.